J Nanopart Res (2024) 26:96
https://doi.org/10.1007/s11051-024-06009-z

RESEARCH

Alteration of magnetic behavior of $(Mg_{0.9}Ni_{0.1}O)_x/(CoFe_2O_4)_{1-x}$ nanocomposites

Majed Sharrouf · R. Awad · Khulud Habanjar

Received: 3 March 2024 / Accepted: 1 May 2024 / Published online: 7 May 2024

Abstract Nanocomposites of $(Mg_{0.9}Ni_{0.1}O)_x/(CoFe_2O_4)_{1-x}$, with $0 \leq x \leq 1$ in weight fractions, were synthesized through the co-precipitation method followed by high-speed ball milling. The investigation of the structural, optical, and magnetic properties was conducted for the synthesized samples. X-ray diffraction (XRD) analysis confirmed the formation of $CoFe_2O_4$ and $Mg_{0.9}Ni_{0.1}O$ distinct phases in the nanocomposites without any detectable impurities or minor phases. Transmission electron microscopy (TEM) and high-resolution TEM (HRTEM) revealed the presence of spherical particles in both the individual phases and their nanocomposites. Raman spectroscopy exhibited strong, well-defined modes for $CoFe_2O_4$, indicating its spinel phase formation, while $Mg_{0.9}Ni_{0.1}O$ displayed two broad peaks (G and D bands). X-ray photoelectron spectroscopy (XPS) was utilized to analyze the elemental compositions and oxidation states (Co^{2+}, Fe^{2+}, Fe^{3+}, Mg^{2+}, Ni^{2+}, and O^{2-}). The magnetic measurements revealed the soft ferromagnetic behavior of pure cobalt ferrite and a combination of weak ferromagnetism and paramagnetic behavior at high magnetic fields for pure $Mg_{0.9}Ni_{0.1}O$.

Keywords $CoFe_2O_4$ · $Mg_{0.9}Ni_{0.1}O$ · Nanocomposites · HRTEM · Paramagnetic · Ferromagnetic

M. Sharrouf · K. Habanjar (✉)
Physics Department, Beirut Arab University, Beirut, Lebanon
e-mail: k.habanjar@bau.edu.lb

R. Awad
Physics Department, Alexandria University, Alexandria, Egypt

R. Awad
Department of Basic Sciences, Faculty of Computer Science and Artificial Intelligence, Pharos University, Alexandria, Egypt

Introduction

Spinel ferrites have a compact cubic lattice structure and are represented by the generic formula MFe_2O_4, with the valence cation M^{2+} including Co, Fe, Cu, etc. Research has been done on spinel ferrites due to their wide range of applications like permanent magnets, power electronics, high-temperature environments, and various industrial applications [1]. Mallesh et al. [2] studied the effect of Ni substitution and annealing temperature on the structural and magnetic properties of MnZn-Ferrites and found that its magnetic characteristics were enhanced with Ni doping. Cobalt ferrite ($CoFe_2O_4$) is classified as one of the best alloys among ceramic materials [3], outperforming other ferrites with its high coercivity, low saturation magnetization, and physical and chemical stability [4]. Moreover, the major characteristics that make them a more promising material include their mechanical hardness, controlled particle sizes, inexpensive, and simple synthesis techniques [4].

One of the most intriguing classes of novel materials is ferrite/oxide nanocomposites, which combine the remarkable nanoscale characteristics of oxide materials with various ferrite components. These materials have received a lot of interest recently due to their remarkable combination of chemical, electrical, and magnetic properties [2, 5–11]. This feature makes them highly recommended and suitable for many applications, such as electronics, energy storage, catalysis, and medicine. Artus et al. [12] reported the alteration of $CoFe_2O_4$ properties when embedded in a NiO matrix via the polyol method. The results showed an enhancement in the magnetic properties in the considered nanocomposites when compared to $CoFe_2O_4$ nanoparticles. Mısırlıoğlu et al. [13] reported adjustable dielectric parameters when adding MgO nanoparticles in cobalt ferrite-based nanocomposites. This may prove beneficial for different applications in the low-frequency domain and upcoming biological uses. Mohan et al. [14] reported a way to overcome the superparamagnetic behavior of nanoscale materials in $CoFe_2O_4$/NiO nanocomposites via exchange bias. The core–shell geometric magnetic nanocomposite systems' interfacial exchange anisotropy was used to explain this. Furthermore, it has been discovered that the auto-combustion approach of mixing cobalt ferrite with CoO nanoparticles changes its magnetic behavior [15]. Another study was done by Mallesh et al. [16] on thermal stability and magnetic properties of $MgFe_2O_4$@ZnO nanoparticles. In this study, it was found that an optimum amount of ZnO-coated MgFO NPs for samples annealed in the temperature range 500 °C-1000 °C can lead to an improvement in magnetic behavior compared to that of MgFO samples.

Characterized by its stability and safety, magnesium oxide (MgO) is a metal oxide used in a variety of applications [17, 18]. MgO has important characteristics at the nanoscale regime, including low electrical conductivity, catalytic activity, and thermal stability [19, 20]. Furthermore, transition metals doped MgO have gained a lot of attention since these dopants can influence MgO's electrical conductivity, catalytic activity, and magnetic behavior, opening doors to a wide array of applications. For instance, Co/Ni-doped MgO is used in novel emitters to control the emissivity of MgO host lattice into selective and concentrated wavelengths [21]. Additionally, the direct band gaps of NiO and MgO are 3.7 eV [22] and 7.8 eV [23], respectively, and this allows $Mg_xNi_{1-x}O$ to have an absorption edge that may be extended from 160 to 335 nm. Therefore, $Mg_xNi_{1-x}O$ in high-efficiency solar-blind UV detectors seems promising. Also, magnetization can be improved by doping unpaired 3d (or 4f) electrons of Fe, Co, and Ni that can cause two times more powerful magnetization than pure MgO to occur in these types of compounds [24]. Furthermore, Almontasser et al. [25] studied the effect of Ni, Co, and Fe dopants in the MgO crystal lattice, resulting in drastic changes in the properties of MgO nanoparticles like an increase in the magnetic properties and enhancement in the antibacterial activity. For that reason, we intended to use Ni-doped MgO as it holds significant importance over pure MgO due to its tailored and enhanced properties.

In this work, a unique method of adding $Mg_{0.9}Ni_{0.1}O$ to a nanocomposite matrix to improve the characteristics of $CoFe_2O_4$ nanoparticles was introduced. The main aim is to investigate the synergistic effects and customize the physical and chemical properties of the resultant nanocomposite by adjusting the composition ratio (x) of $Mg_{0.9}Ni_{0.1}O$ and $CoFe_2O_4$, denoted as $(Mg_{0.9}Ni_{0.1}O)_x/(CoFe_2O_4)_{1-x}$. This approach presents prospects for controlling structural, electrical, and magnetic properties, opening doors for applications in a range of domains including environmental cleanup, biological imaging, catalysis, and magnetic storage. This research advances the knowledge of the interactions between nanoparticles in composite materials and creates new avenues for the development of functional nanocomposites with adjustable features. The structure, morphology, and elemental compositions were tested. Moreover, the effect of adding $Mg_{0.9}Ni_{0.1}O$ nanoparticles on the magnetic behavior of soft ferromagnetic $CoFe_2O_4$ was also investigated and discussed.

Experimental technique

The wet chemical co-precipitation method was used to prepare pure $CoFe_2O_4$ and $Mg_{0.9}Ni_{0.1}O$ nanoparticles. For the synthesis of $CoFe_2O_4$ nanoparticles, 1 M iron (III) chloride hexahydrate ($FeCl_3.6H_2O, \geq 98\%$, Sigma-Aldrich) and 1 M of cobalt chloride hexahydrate ($CoCl_2 \bullet 2H_2O, \geq 98\%$, Sigma-Aldrich) solutions were prepared by using deionized water as dispersing solvent. Both solutions were mixed and subjected to continuous magnetic stirring at room temperature.

To adjust the solution at a highly basic condition (pH = 13), a solution of 4 M NaOH was added dropwise to the solution. Afterwards, the reaction was stirred for 2 h at 80 °C. The resultant precipitate was subjected to a continuous washing process with deionized water to remove the residues until the pH was 7 and then dried at 100°C for 16 h in air. For the synthesis of $Mg_{0.9}Ni_{0.1}O$ nanoparticles, 1 M of magnesium chloride hexahydrate ($MgCl_2.6H_2O, \geq 99\%$, Sigma-Aldrich) and 1 M nickel chloride hexahydrate ($NiCl_2 \bullet 6H_2O$, Sigma-Aldrich, ≥ 98) solutions were prepared, mixed, and subjected to continuous magnetic stirring at room temperature. Afterward, the pH was increased to 12 by dropping a 4 M NaOH solution, followed by a stirring process for 6 h at room temperature until a precipitate was formed. The resultant product was washed with 50% deionized water and 50% ethanol until the pH became neutral. The powder obtained was dried at 80 °C for 12 h in air.

For the synthesis of nanocomposites $(Mg_{0\cdot 9}Ni_{0.1}O)_x/(CoFe_2O_4)_{1-x}$, the resultant powders of both nanoparticles were mixed via high-speed ball milling method, with x = 0.1, 0.2, 0.4 and 0.8 named as CM10, CM20, CM40, and CM80, respectively. Different percentages of $CoFe_2O_4$ and $Mg_{0.9}Ni_{0.1}O$ were weighed and then ball milled via PM 100 Planetary Ball Milling machine. The ball-to-powder weight ratio used was 5:1 at a speed of 300 rpm for 10 min. Finally, the six samples were calcined at 700°C for 4 h.

X-ray diffraction (XRD) patterns were acquired using a Bruker D8 Advance powered diffractometer, utilizing Cu-kα radiation (λ = 1.5406 Å). The scanning speed employed was 3°/min within the $20° \leq 2\theta \leq 80°$ range. The shape and the size of the prepared nanoparticles, as well as HRTEM images, were obtained using the JEM 100 CX Transmission Electron microscope (TEM). The images provided magnification from 100× to 250,000× with a resolution of 1 Å, operating at a voltage of 80 kV. Raman spectra were gathered using a Raman spectrometer (Model: SENTERRA, BRUKER OPTICS). The utilized wavelength was λ = 659 nm, with an output power of 20W. The parameters consisted of a continuous mode time of 10 s, a snapshot time of 7 s, 30 accumulations, and a 100× microscope objective lens. X-ray photoelectron spectroscopy (XPS) data were collected on a *k*α instrument (ThermoFisher Scientific, USA) utilizing monochromatic X-ray *Al-k*α radiation, covering an energy range of 10 to 1350 eV. The spot size was 400 μ*m*, and the measurement was performed at a pressure of 10^{-9} mbar. For full survey XPS spectra, the pass energy was set at 200 eV, while high-resolution XPS spectra used a pass energy of 50 eV. The binding energy scale was calibrated using standard silver (Ag) and gold (Au) sheets. Magnetic hysteresis loops were examined using a Lakeshore 7410 VSM. The magnetic field varied from -20,000 G to + 20,000 G, and the measurements were conducted at room temperature.

Results and discussion

Figure 1 shows the experimental and the refined XRD patterns of $CoFe_2O_4$, $Mg_{0.9}Ni_{0.1}O$, and their nanocomposites CM10, CM20, CM40 and CM80. The peaks of $CoFe_2O_4$ match the (111), (220), (311), (222), (400), (422), (511), (440), (620), and (533) reflections of the cubic spinel structure with space group $Fd\bar{3}m$ [26], as revealed by MAUD refinement. For the $Mg_{0.9}Ni_{0.1}O$ phase, the peaks (111), (200), (220), (311), and (222) are all related to MgO, confirming the incorporation of Ni ions in the cubic structure of MgO with space group $Fm\bar{3}m$ [27]. This verifies the purity of both nanoparticles without the formation of any impurity. As for the nanocomposites, all the peaks shown are related to $CoFe_2O_4$ and $Mg_{0.9}Ni_{0.1}O$ without the formation of any secondary phases with crystal structures different than the two main phases. It is well known, for the $CoFe_2O_4$ pattern, that the ratio of the intensities of the two peaks (220) and (222) (I_{220}/I_{222}) depends on the cation distribution in the crystal structure [28–30]. For that reason, the ratio I_{220}/I_{222} was calculated for x = 0, 0.1, 0.2, 0.4, and 0.8, and plotted as a function of x in Fig. 2. The drastic change in this ratio could be a sign of the redistribution of cations between tetrahedral and octahedral sites [31].

The lattice parameter '*a*' for the two phases, the microstrain and the crystallite size were extracted from MAUD and tabulated in Table 1. For pure $CoFe_2O_4$ and pure $Mg_{0.9}Ni_{0.1}O$, *a* is 8.373 Å and 4.204 Å, respectively. The two values are consistent with the literature [25, 32]. However, the lattice parameters of the two phases, in the four nanocomposites, changed oppositely with the microstrain as reported by Qin et al. [33]. The crystallite sizes for $CoFe_2O_4$ and $Mg_{0.9}Ni_{0.1}O$ were calculated using

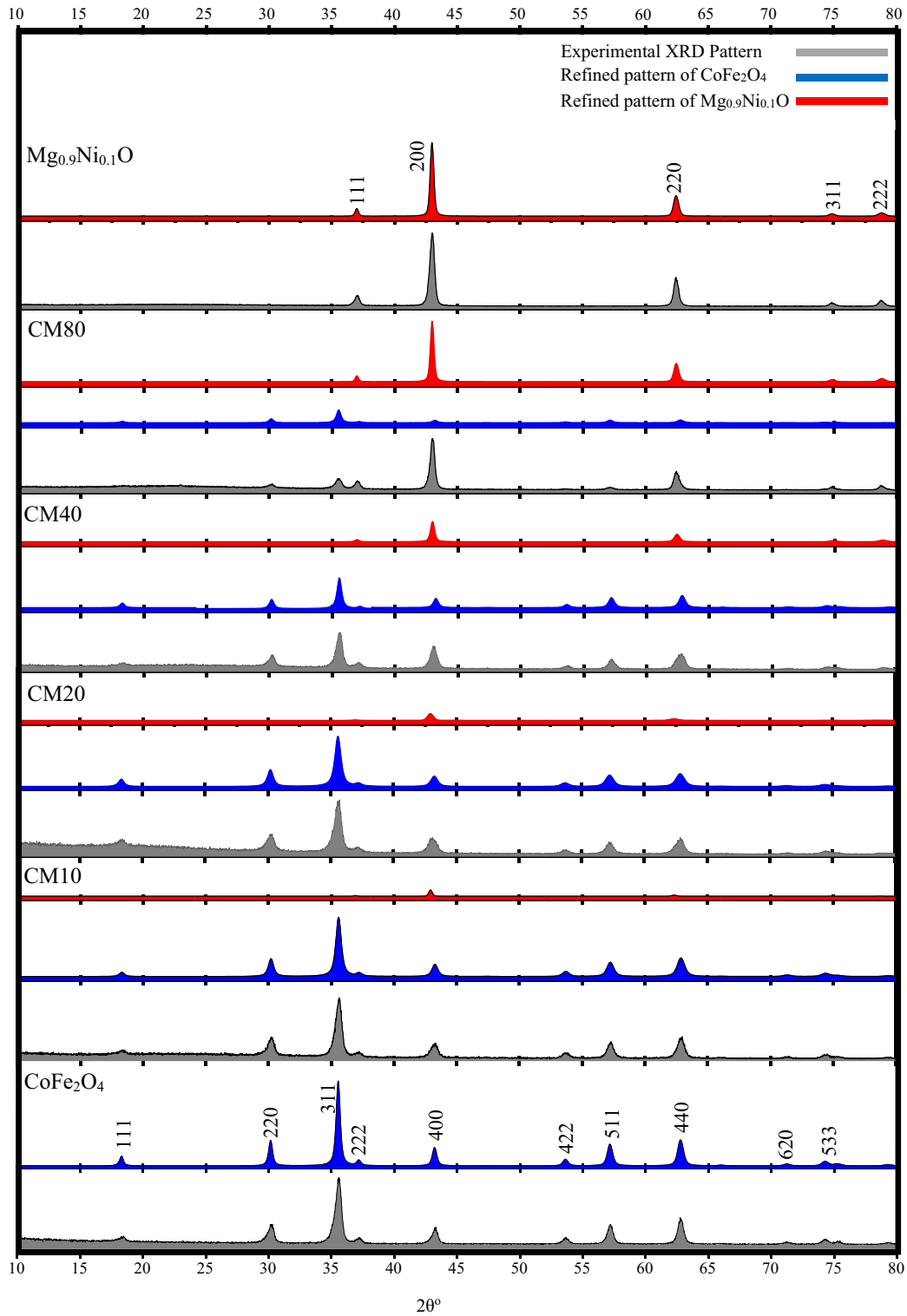

Fig. 1 Stack plot of the XRD patterns of $(Mg_{0.9}Ni_{0.1}O)_x/(CoFe_2O_4)_{1-x}$ (x = 0, 0.1, 0.2, 0.4, 0.8 and 1) showing the experimental pattern with the refined pattern for each of $CoFe_2O_4$ and $Mg_{0.9}Ni_{0.1}O$ phases in the six samples

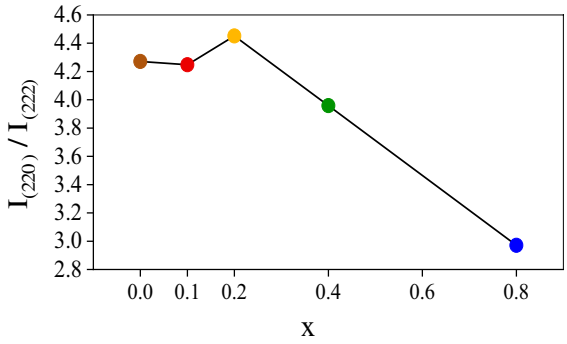

Fig. 2 The ratio $I_{(220)}/I_{(222)}$ of $CoFe_2O_4$ phase as a function of x

Debye–Scherrer's equation and found to be 14.61 nm and 19.22 nm respectively [34, 35]. For the nanocomposites, the crystallite size of the $CoFe_2O_4$ phase decreased from x = 0 till x = 0.2, then increased from x = 0.2 till x = 0.8 as seen in Table 1. The effects of incorporating MgO into $CoFe_2O_4$ suggested that adding non-magnetic MgO with low concentration changes the degree of magnetic $CoFe_2O_4$ aggregation which reduces the crystallite size of $CoFe_2O_4$ and increases that of MgO [36].

Figure 3 displays TEM images along with HRTEM micrographs for $CoFe_2O_4$, CM40, and $Mg_{0.9}Ni_{0.1}O$. The $CoFe_2O_4$ nanoparticles show a rounded morphology with an average particle size of 14.7 nm [37]. The HRTEM image affirms the good crystallinity of these nanoparticles, characterized by the preferred orientation of (311) planes [38]. Similarly, $Mg_{0.9}Ni_{0.1}O$ nanoparticles also exhibit nearly spherical shapes, with an average particle size of 40.9 nm. The HRTEM micrograph shows the presence of preferred (200) planes in these nanoparticles [39]. As for the four nanocomposites, they all exhibit spherical shapes with wider size distribution than the pure phases and average particle sizes of 25.4 nm, 31.3 nm, 33.2 nm, 33.2 nm, and 56.6 nm for CM10, CM20, CM40, and CM80, respectively. The HRTEM micrograph of CM40 nanocomposite, in Fig. 3b, revealed the coexistence of the two phases with an identified plane for each of $CoFe_2O_4$ and $Mg_{0.9}Ni_{0.1}O$ phases [36].

An analytical method for determining the vibrational energy modes of nanoparticles to characterize materials is Raman spectroscopy. When molecules interact with electromagnetic radiation, the Raman spectrum is produced. Room temperature Raman spectra of $CoFe_2O_4$, $Mg_{0.9}Ni_{0.1}O$, and CM40 nanocomposite are shown in Fig. 4 in the range of 250—2500 cm^{-1}. According to the group theory, $CoFe_2O_4$ spinel ferrite has five Raman active modes: A_{1g}, E_g, and $3T_{2g}$, which are attributed to the oxygen of A-site and B-site ions in the spinel structure [40]. A_{1g} modes (> 600 cm^{-1}) are associated with the symmetric stretching of oxygen anions with tetrahedral cations, whereas E_g and T_{2g} modes (< 600 cm^{-1}) are due to symmetric and antisymmetric bending of oxygen anions with octahedral cations [41]. In our study, $CoFe_2O_4$ showed four distinct peaks at 475, 568, 617, and 686 cm^{-1} that can be assigned to $T_{2g}(2)$, $T_{2g}(1)$, $A_{1g}(2)$, and $A_{1g}(1)$, respectively [42]. The splitting of the A_{1g} band into $A_{1g}(2)$ and $A_{1g}(1)$ peaks is a typical feature for inverse and mixed spinel ferrites [43]. This result is similar to

Table 1 Lattice parameters and crystallite size of $CoFe_2O_4$ and $Mg_{0.9}Ni_{0.1}O$

x	Phase	*a* (Å)	Error × 10^{-4}	Microstrain × 10^{-4}	Error × 10^{-5}	Crystallite size (nm)
0	$CoFe_2O_4$	8.373	16.7	15.7	3.6	14.61
	$Mg_{0.9}Ni_{0.1}O$	-----	-----	-----	-----	-----
0.1	$CoFe_2O_4$	8.360	13.8	17.4	7.1	14.26
	$Mg_{0.9}Ni_{0.1}O$	4.208	5.5	8.21	14.2	----
0.2	$CoFe_2O_4$	8.357	12.7	17.8	7.0	12.46
	$Mg_{0.9}Ni_{0.1}O$	4.208	5.5	9.2	15.2	13.25
0.4	$CoFe_2O_4$	8.364	11.6	15.3	8.1	13.75
	$Mg_{0.9}Ni_{0.1}O$	4.206	6.7	19.2	14.9	14.18
0.8	$CoFe_2O_4$	8.370	18.2	14.4	7.5	14.56
	$Mg_{0.9}Ni_{0.1}O$	4.205	6.4	20.0	6.6	18.09
1	$CoFe_2O_4$	-----	-----	-----	-----	----
	$Mg_{0.9}Ni_{0.1}O$	4.204	4.4	18.3	3.4	19.22

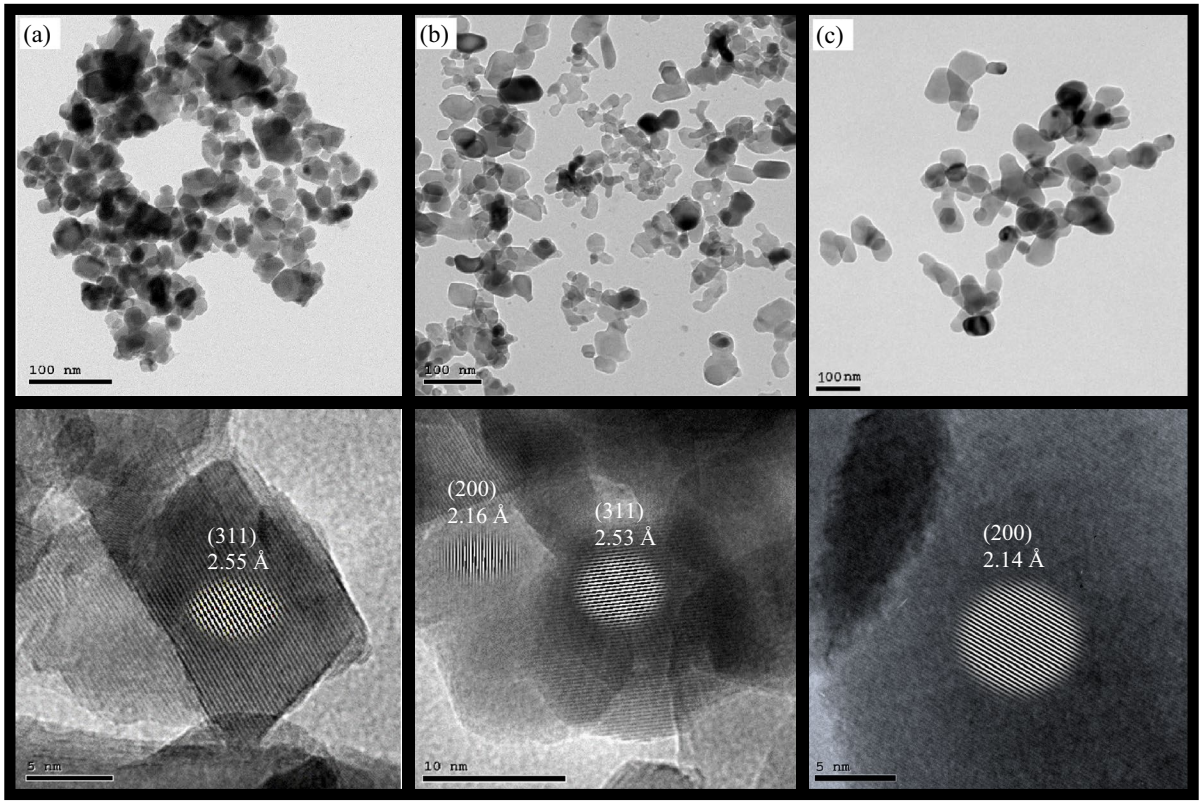

Fig. 3 TEM image and HRTEM micrograph for (**a**) $CoFe_2O_4$, (**b**) CM40 nanocomposite and (**c**) $Mg_{0.9}Ni_{0.1}O$

the study reported by Kumar et al. [42] for $CoFe_2O_4$ nanoparticles synthesized by the thermal decomposition approach. The Raman spectrum for pure $Mg_{0.9}Ni_{0.1}O$ showed a peak with high intensity around 1374 cm^{-1} and another lower peak at 1904 cm^{-1}. This result is comparable to the one reported by Weible et al. [44]. Also, Athar et al. [45] reported that the peak below 1500 cm^{-1} is associated with D-band, whereas, the peak above 1500 cm^{-1} is for the G-band of MgO nanoparticles. As for the CM40 nanocomposite, all the peaks corresponding to $CoFe_2O_4$ are observed with a significant shift for A_{1g} modes and a change in peak intensities as seen in Fig. 4. Also, the peak at 1374 cm^{-1} of $Mg_{0.9}Ni_{0.1}O$ still exists with lower intensity. To go deeper into results, the spectra of $CoFe_2O_4$ and CM40 were deconvoluted into Gaussian peaks and shown in Fig. 5. Accordingly, the $T_{2g}(2)$ peak in CM40 nanocomposite is split into two different peaks positioned at 469 cm^{-1} and 497 cm^{-1}. As reported by Ortiz et al. [46], the cation redistribution between tetrahedral and octahedral sites can alter the symmetry of the crystal structure leading to the formation of new vibrational modes, and this redistribution is confirmed in the XRD analysis. According to a study done by Suthar et al. [47] on Mg-doped $CoFe_2O_4$ thin films, a blue shift is observed in $A_{1g}(1)$ peak when Mg^{2+} ions were incorporated in $CoFe_2O_4$, as Mg^{2+} prefers to sit in tetrahedral sites. Another study was done by Tong et al. [48] on Ni-doped $CoFe_2O_4$. They found that all the peaks were red-shifted upon the incorporation of Ni^{2+} ions in $CoFe_2O_4$. As a result, the change in the peak positions of Ag modes might be due to the incorporation of Ni^{2+} and Mg^{2+} ions in $CoFe_2O_4$. Moreover, it is reported by many researchers that $T_{2g}(2)$ and $A_{1g}(1)$ peaks are almost due to the Co^{2+} ions at octahedral and tetrahedral sites, respectively [40, 49]. Figure 6 shows the spectra of $CoFe_2O_4$ and CM40 drawn on the same scale. It is seen that the area of the $T_{2g}(2)$ peak relative to $A_{1g}(1)$ decreased significantly from $CoFe_2O_4$ to CM40. This is another evidence for the migration of Co^{2+} cations from the octahedral to tetrahedral sites [37].

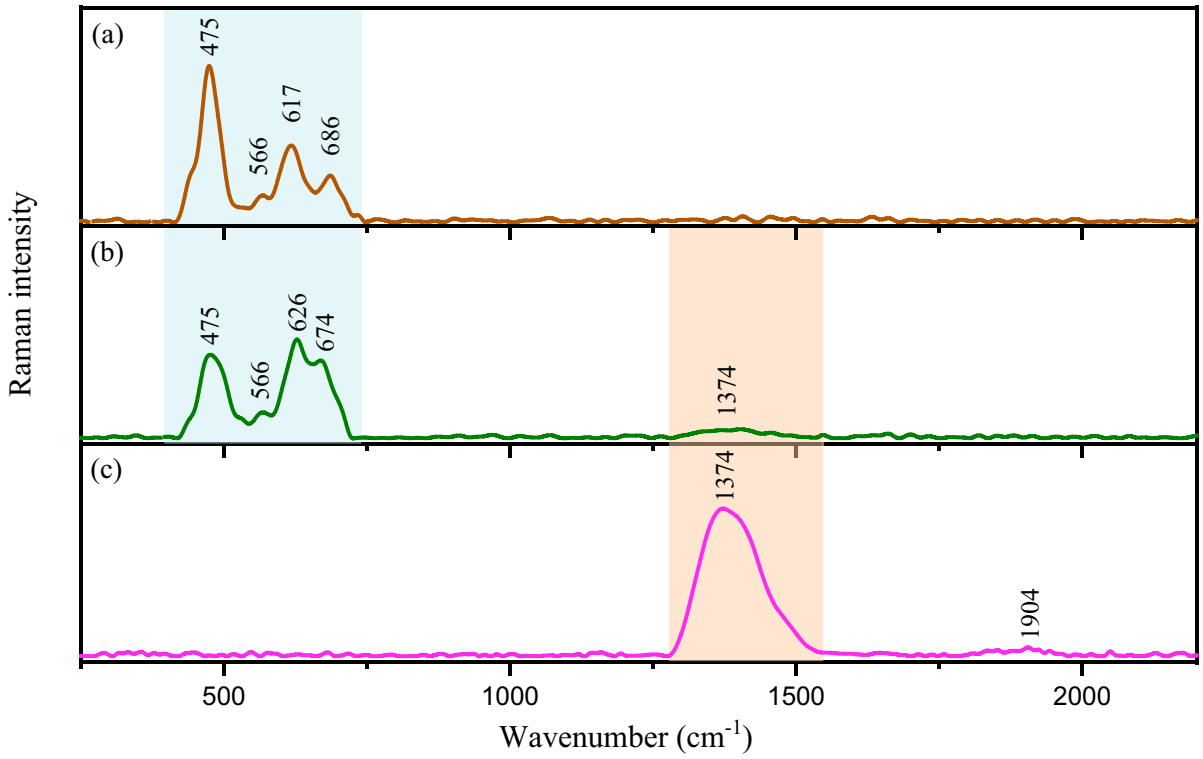

Fig. 4 Raman spectra of (**a**) $CoFe_2O_4$ (x = 0), (**b**) CM40 and (**c**) $Mg_{0.9}Ni_{0.1}O$

The chemical states and elemental compositions were identified by XPS full scan spectra of $CoFe_2O_4$, $Mg_{0.9}Ni_{0.1}O$, and the CM40 nanocomposite as shown in Fig. 7. The survey spectrum for the pure $CoFe_2O_4$ phase confirms the existence of Co, Fe, and O, whereas $Mg_{0.9}Ni_{0.1}O$ spectrum revealed the existence of Mg, Ni, and O. As for the CM40 nanocomposite, the XPS spectrum showed the signals for all the elements without additional spectral lines, confirming the purity of the nanocomposite sample. In addition, Co2p, Fe2p, O1s, Mg1s, and Ni2s peaks are obtained from High-resolution HR-XPS and deconvoluted to determine their oxidation states as shown in Fig. 8. The results for the binding energies and areas are also recorded in Table 1. The Co2p spectrum, in $CoFe_2O_4$ and CM40, showed two main peaks that correspond to $Co2p_{3/2}$ and $Co2p_{1/2}$, respectively [50]. The energy difference between these two peaks is found to be 15.3 eV, confirming the + 2 oxidation state of the Co ions [51]. The deconvolution of $Co2p_{3/2}$ and $Co2p_{1/2}$, Fig. 8a, revealed the splitting of each peak into two minor peaks attributed to Co ions in octahedral (A) and tetrahedral (B) sites. The two other peaks at 787.9 eV and 803.4 eV in pure $CoFe_2O_4$ are known as satellite peaks related to the shake-up type of $Co2p_{3/2}$ and $Co2p_{1/2}$ edge [52]. Figure 8b shows the Fe2p spectra in $CoFe_2O_4$ and CM40 nanocomposites. The two spectra revealed the two main peaks belonging to $Fe2p_{3/2}$ and $Fe2p_{1/2}$. The deconvolution of the two Fe2p spectra suggested the existence of Fe^{2+}- $2p_{3/2}(O_h)$, Fe^{3+}- $2p_{3/2}(T_h)$, Fe^{2+}- $2p_{1/2}(O_h)$ and Fe^{3+}- $2p_{1/2}(T_h)$ peaks [53]. Thus, Fe ions exist in both sites of the crystal structure in $CoFe_2O_4$ and CM40. The O1s peak, in Fig. 8c, is deconvoluted into three common peaks among the three nanocomposites. The peak of lowest binding energy (~ 530 eV) is attributed to lattice oxygen, whereas the peaks around 532 eV and 535 eV belong to C-O/C = O and the hydroxyl group (OH) at the surface, respectively [54]. The Mg1s peak was deconvoluted into two peaks at around 1303 eV and 1305 eV, which are attributed to Mg^{2+} in MgO lattice and $Mg(OH)_2$ formed on the surface of the nanoparticles, respectively [55]. The deconvolution of the Ni2p peak revealed two main

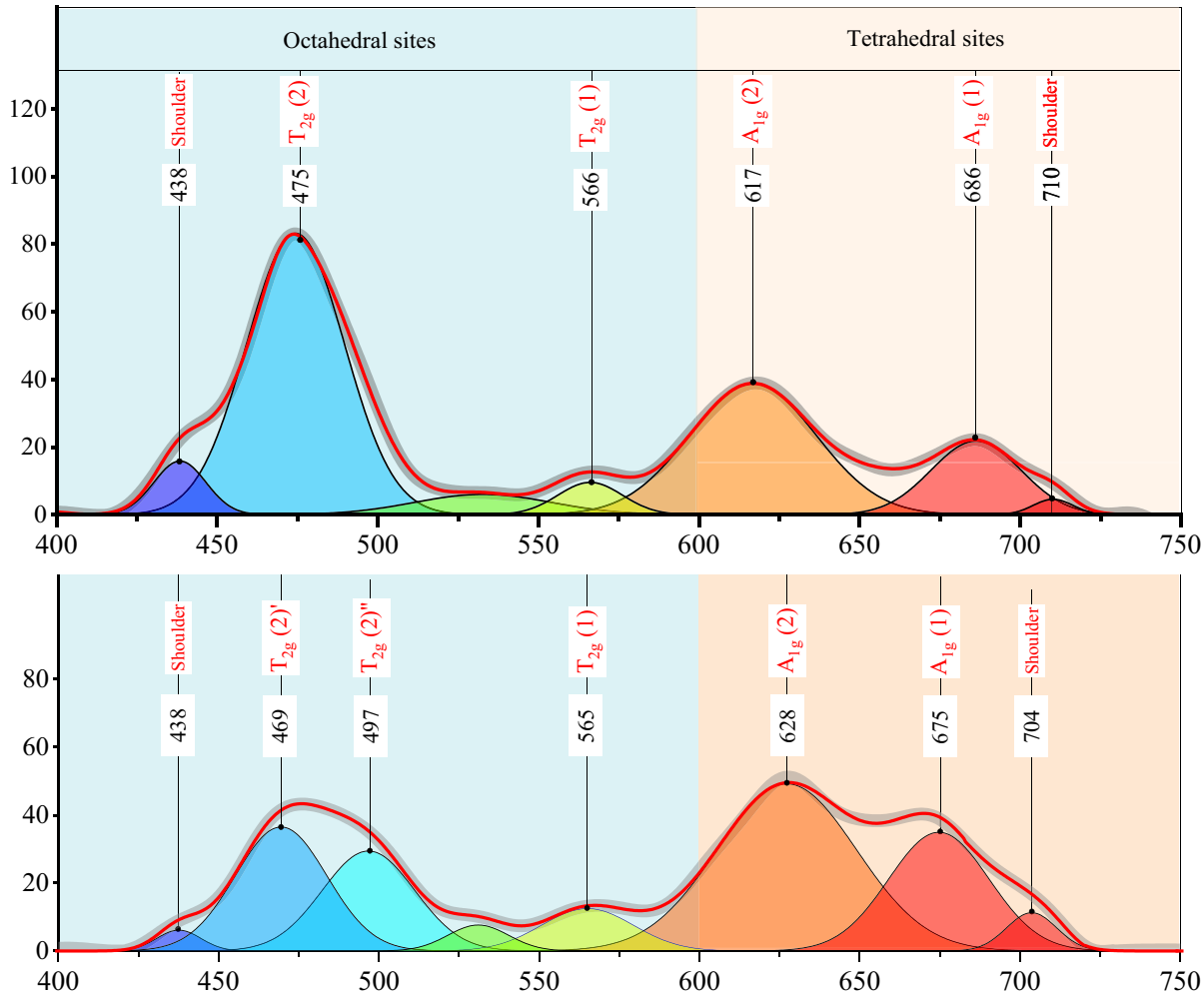

Fig. 5 Deconvoluted Raman spectra of (**a**) $CoFe_2O_4$ and, (**b**) CM40 nanocomposite

peaks, Ni-$2P_{3/2}$ and Ni-$2p_{1/2}$ that confirmed the + 2 oxidation state of Ni as reported by Yang et al. [56].

To obtain insight into the cation distribution in the crystal structure of $CoFe_2O_4$, the area of the corresponding peaks in Table 2 is used to estimate the percentages of Co and Fe ions occupying tetrahedral and octahedral positions. The general chemical formula of the mixed spinel $CoFe_2O_4$ can be written as $(Co^{2+}{}_{\delta}Fe^{3+}{}_{1-\delta})^{A}(Co^{2+}{}_{1-\delta}Fe^{3+}{}_{1+\delta})^{B}O_4$ [57]. The type of spinel ferrite depends on the value of δ so that the inverse structure is represented by $\delta = 0$ and the normal structure has $\delta = 1$. However, for $0 < \delta < 1$, the structure is mixed spinel. The chemical distribution formulas obtained for $CoFe_2O_4$ in pure $CoFe_2O_4$ and CM40 are $(Co^{2+}{}_{0.29}Fe^{3+}{}_{0.63})^{A}(Co^{2+}{}_{0.71}Fe^{3+}{}_{1.37})^{B}O_4$ and $(Co^{2+}{}_{0.40}Fe^{3+}{}_{0.70})^{A}(Co^{2+}{}_{0.60}Fe^{3+}{}_{1.30})^{B}$, respectively. The δ value increases from 0.29 to 0.40 which confirms the redistribution of Co^{2+} between octahedral to tetrahedral sites. This conclusion is in excellent agreement with the findings of Raman and XRD analyses, which showed that some Co^{2+}ions moved from octahedral to tetrahedral positions. According to Li et al. [58], this conclusion is thought to have a significant impact on magnetic characteristics.

To study the magnetic properties of the prepared samples $(Mg_{0\cdot9}Ni_{0.1}O)_x/(CoFe_2O_4)_{1-x}$, (x = 0, 0.1, 0.2, 0.4, 0.8 and 1), M-H hysteresis loops were investigated at room temperature with varying magnetic field between -20,000 G and 20,000 G, as shown in

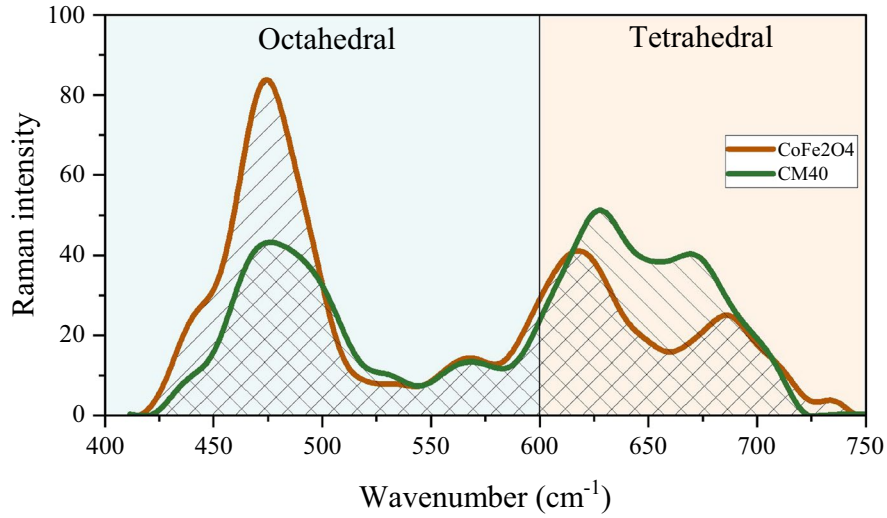

Fig. 6 Raman spectra of $CoFe_2O_4$ and CM40 nanocomposite drawn in the same scale

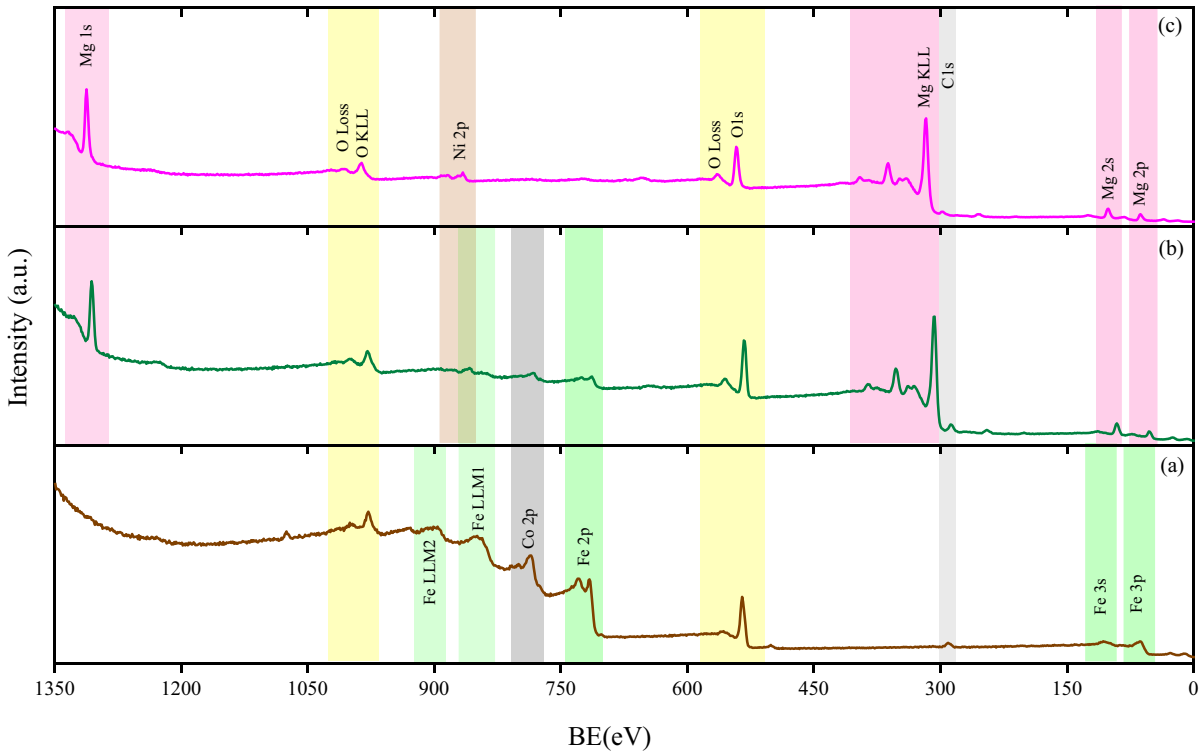

Fig. 7 High resolution XPS survey spectra of (**a**) $CoFe_2O_4$, (**b**) $Mg_{0.9}Ni_{0.1}O$ and (**c**) CM40 nanocomposite

Fig. 9. $CoFe_2O_4$ showed soft ferromagnetic behavior as reported by many researchers [46, 57, 59]. This behavior can be attributed to magnetic ordering in $CoFe_2O_4$ due to the presence of Co^{2+} ions in the octahedral sites as reported by Hammad et al. [60]. This is also confirmed by XPS and Raman analysis. On the other hand, $Mg_{0.9}Ni_{0.1}O$ nanoparticles showed very weak ferromagnetism, compared to $CoFe_2O_4$, with paramagnetic behavior at magnetic fields $H > 5000$ G. Similar results were observed by

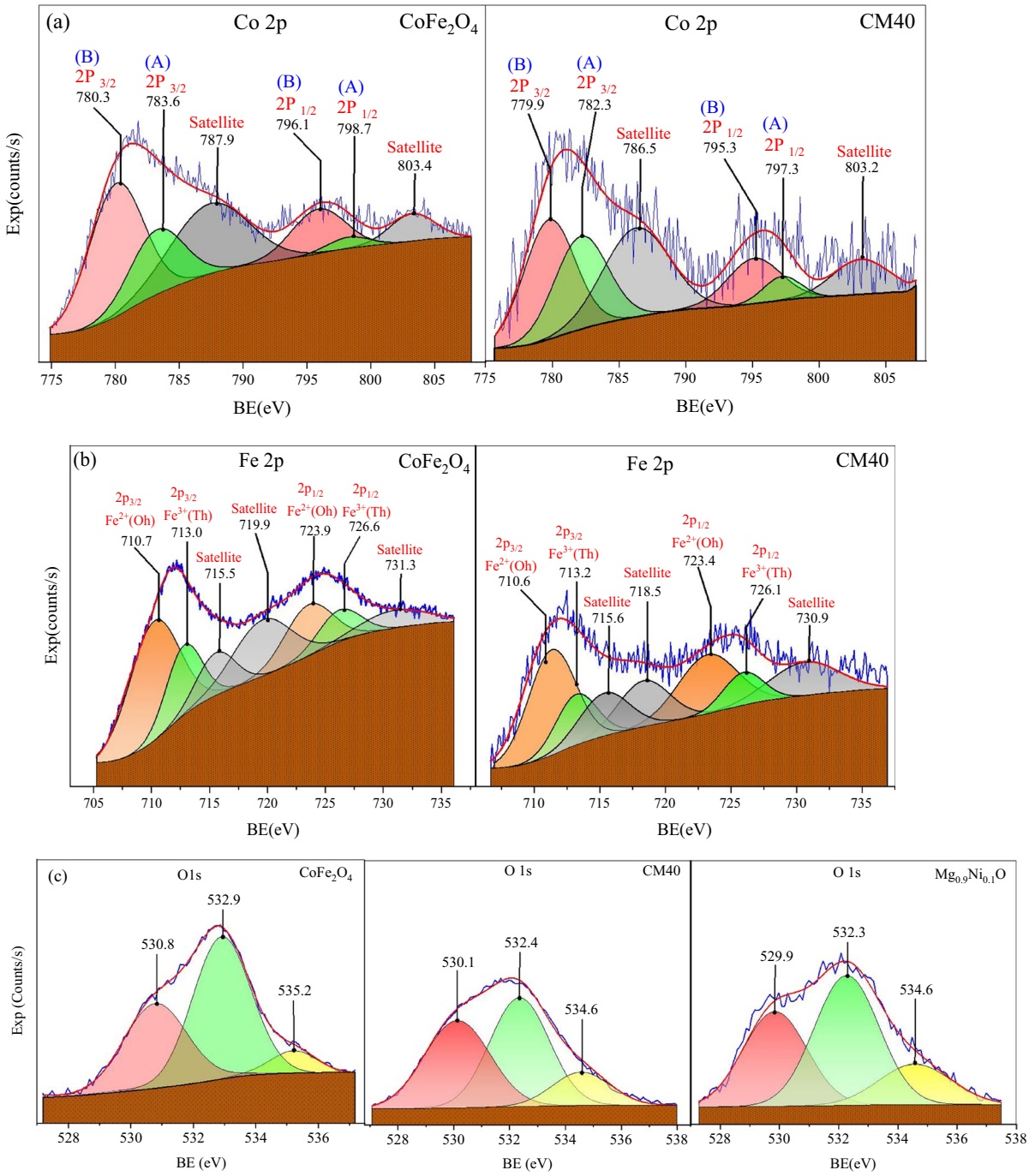

Fig. 8 The deconvolution of the main spectra lines of (**a**) Co-2P, (**b**) Fe-2p, (**c**) O-1s (**d**) Mg-1s and (**e**)Ni-2P

Almontasser et al. [25], who reported that $Mg_{1-x}Ni_xO$ nanoparticles were transferred from paramagnetic in pure MgO to ferromagnetic and paramagnetic in 7% Ni-doped MgO. This transition was ascribed to the influence of Mg and O vacancies at the surface of the nanoparticles. Another study was performed by Narayan et al. [61] on 0.5 at% of Ni-doped MgO nanoparticles and found that it behaves as a

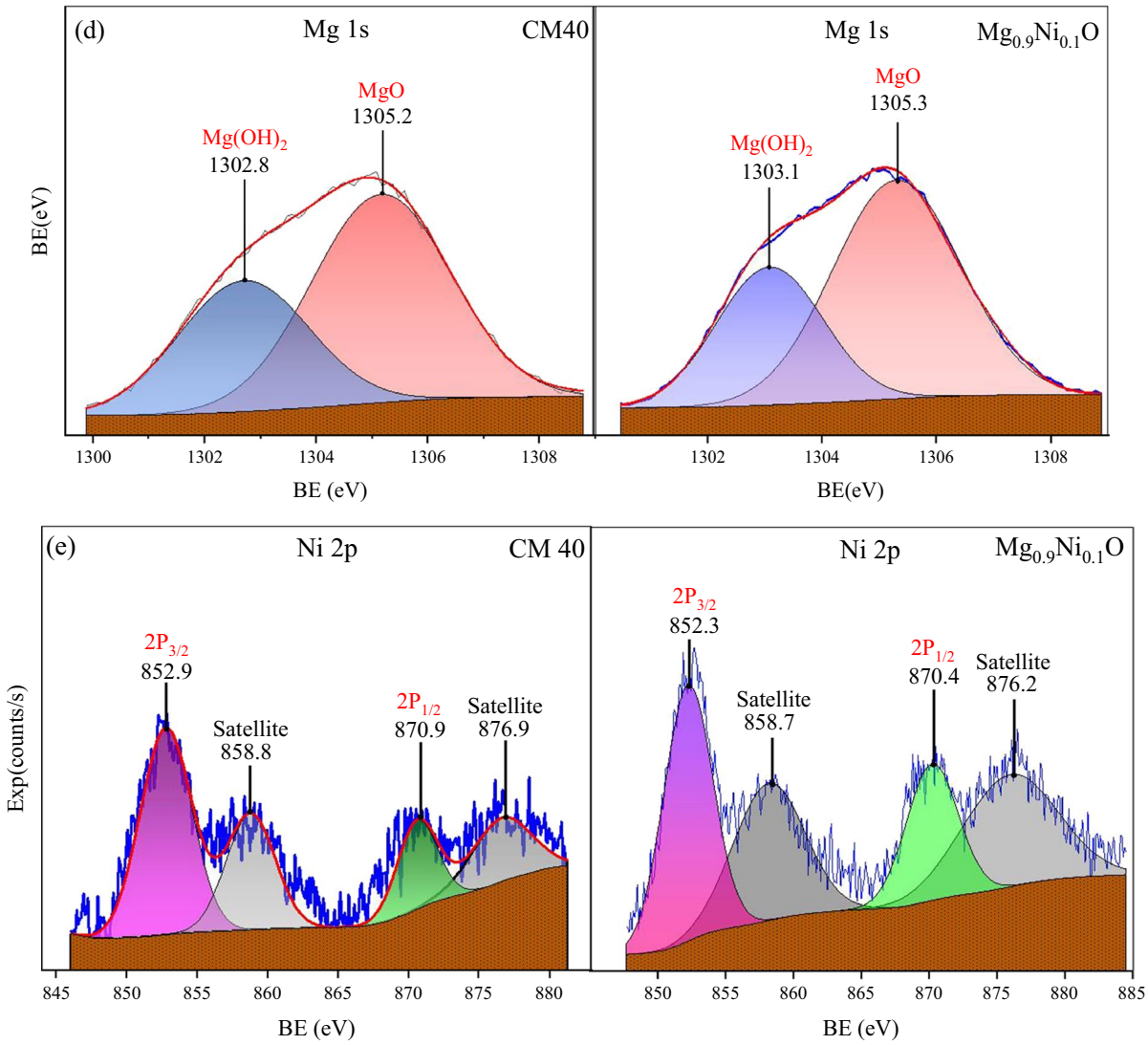

Fig. 8 (continued)

paramagnetic material. They suggested that doping impurities in a doubly ionized state (Ni^{2+}) can have partially 3d shells with unpaired spins that result in a magnetic moment. On the other hand, there won't be a net magnetic moment and the system functions like a perfect paramagnet when these ions are dispersed randomly in a non-interacting manner throughout the lattice. In this instance, particularly at high magnetic fields, the paramagnetic contribution from the Ni ions might be predominant. Therefore, for the MgO phase, Ni's paramagnetic behavior can prevail over any other magnetic behavior. The four nanocomposites all exhibited ferromagnetic behavior, each with a unique set of magnetic characteristics that will be covered in more detail below.

At high magnetic fields and below Curie temperature, the magnetization may be expressed using Eq. (1) [62]:

$$M = M_s \times [1 - \frac{b}{H^2}] \quad (1)$$

where b is associated with the effective anisotropy constant and obtained from the slope of the M vs $1/H^2$ plots. The magnetization M was plotted versus $1/H^2$

Table 2 The binding energy (BE) and the area of the de-convoluted core energy levels of Co, Fe, O, Mg and Ni in $CoFe_2O_4$, CM40 and $Mg_{0.9}Ni_{0.1}O$

Core energy levels		Assignment	$CoFe_2O_4$		CM40		$Mg_{0.9}Ni_{0.1}O$	
			Eb (eV)	Area	Eb (eV)	Area	Eb (eV)	Area
Co-2p	Co-$2p_{3/2}$	$Co^{2+}(O_h)$	780.3	8917.2	779.9	3065.0	----	----
		$Co^{3+}(T_h)$	783.6	4331.3	782.3	2471.5	----	----
		Satellite	787.9	6779.9	786.5	2933.8	----	----
	Co-$2p_{1/2}$	$Co^{2+}(O_h)$	796.1	2981.6	795.3	1214.9	----	----
		$Co^{3+}(T_h)$	798.7	596.1	797.3	420.8	----	----
		Satellite	803.4	1536.6	803.2	631.4	----	----
Fe-2p	Fe-$2p_{3/2}$	$Fe^{2+}(O_h)$	710.7	14648.1	710.6	5218.1	----	----
		$Fe^{3+}(T_h)$	713.0	6192.4	713.0	2164.9	----	----
		Satellite	715.5	4053.7	715.6	2262.5	----	----
		Satellite	719.9	7588.2	718.5	2683.8	----	----
	Fe-$2p_{1/2}$	$Fe^{2+}(O_h)$	723.9	6005.4	723.4	3497.8	----	----
		$Fe^{3+}(T_h)$	726.6	3307.2	726.1	1580.8	----	----
		Satellite	731.3	2888.1	730.9	2227.1	----	----
O-1s		Lattice O	530.8	6078.6	530.1	18464.2	529.9	20305.3
		C-O/C=O	532.9	9415.2	532.4	24075.7	532.3	25281.7
		OH	535.2	1136.8	534.6	5386.6	534.6	9654.8
Mg-1s		$Mg(OH)_2$	----	----	1302.8	15249.1	1303.1	20316.6
		MgO	----	----	1305.2	25650.8	1305.3	38622.8
Ni-2p	Ni-$2p_{3/2}$	Ni^{2+}	----	----	852.9	4473.7	852.3	7846.8
		Satellite	----	----	858.8	2397.9	858.7	5386.4
	Ni-$2p_{1/2}$	Ni^{2+}	----	----	870.9	1485.0	870.4	2948.6
		Satellite	----	----	876.9	1580.8	876.2	6596.4

for all the samples, as shown in Fig. 10, from which the magnetic saturation (M_s) was estimated by extrapolating the plot to $1/H^2=0$. For $Mg_{0.9}Ni_{0.1}O$, the ferromagnetic magnetization (M_f) was first obtained by subtracting the paramagnetic behavior from the magnetization [63] as seen in the inset of Fig. 9, and the linear fit is shown in Fig. 10b. The retentivity (M_r) and the coercivity (H_c) were obtained from the M-intercept and H-intercept of the M-H loops as seen in Fig. 11. The effective anisotropy constant (k_{eff}) was estimated using the law of approach to saturation (H» H_c) according to Eq. (2) [26]:

$$k_{eff} = \mu_o M_s \sqrt{\frac{15b}{4}} \quad (2)$$

where μ_o is the permeability of free space. The different magnetic parameters M_s, M_r, M_r/M_s, H_c, and K_{eff} are plotted as a function of x in Fig. 12. For $CoFe_2O_4$, $M_s=54.1$ emu/g which is very close to the one reported by Jian et al. [59] for single domain nanoparticles (15.8 nm) prepared by co-precipitation method. The value of M_s is smaller than that of bulk $CoFe_2O_4$ due to the surface disorder or spin canting at the surface of the nanoparticles as reported by Ansari et al. [43]. As for $Mg_{0.9}Ni_{0.1}O$ nanoparticles, $M_s=0.0231$emu/g is similar to the result obtained by Ali et al. [64]. As estimated, the four nanocomposites' saturation magnetization showed a downward trend as the amount of the non-magnetic $Mg_{0.9}Ni_{0.1}O$ increased. Numerous researchers have observed similar outcomes for soft magnetic and nonmagnetic nanocomposites like $CoFe_2O_4$/ZnO [65], $CuFe_2O_4$/MgO [64], and MgO/$MgFe_2O_4$ [66]. Assuming that the saturation magnetization for the nanocomposites is only due to the $CoFe_2O_4$ phase, their saturation magnetization in this assumption is represented by $M_s'=(1-x)M_s(x=0)$ and is plotted in Fig. 12. The values of M_s are lower than M_s' for CM10, CM20 and CM40 nanocomposites. Many factors can affect the saturation magnetization of nanoparticles like the particle size [67] and cation distribution [57]. According to our study, XPS and Raman analysis revealed the migration of Co^{2+} ions

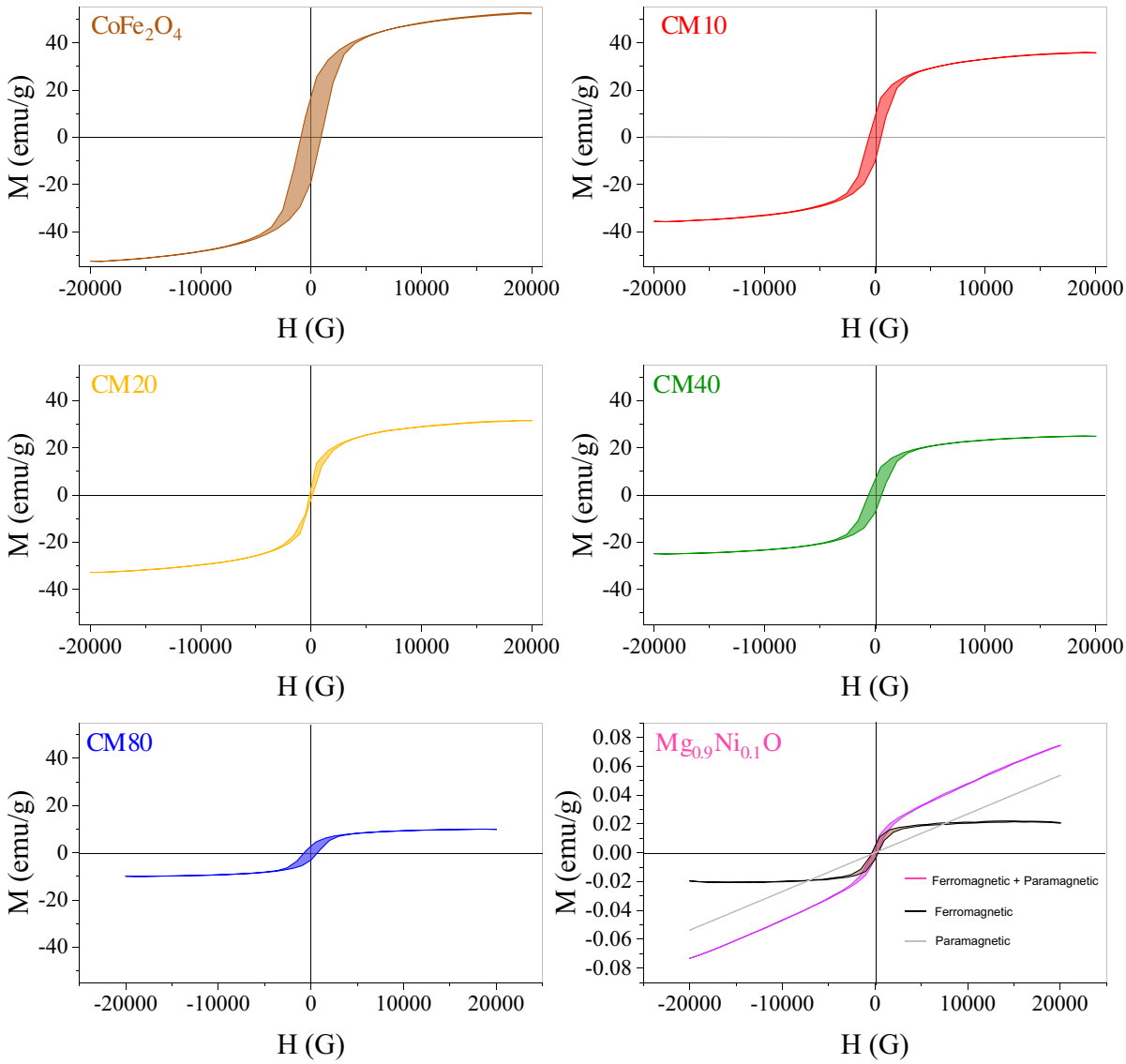

Fig. 9 M-H hysteresis loops of $/(Mg_{0.9}Ni_{0.1}O)_x/(CoFe_2O_4)_{1-x}$ at room temperature

from B sites to A sites in CM40, which could be the reason behind the further reduction in the saturation magnetization as reported by Manh et al. [31]. The coercivity for $CoFe_2O_4$ was found to be $H_c = 912$ Oe, which is similar to the value obtained by Liu et al. [68] for 12 nm particle size. As expected, for relatively low $Mg_{0.9}Ni_{0.1}O$ content, H_c decreases from $x = 0$ till $x = 0.2$ as a result of the decrease in the effective anisotropy as reported by many researchers [67, 69]. However, H_c increases significantly from $x = 0.2$ till $x = 0.8$ for relatively high $Mg_{0.9}Ni_{0.1}O$ content, which is opposite to the trend observed for K_{eff}. It is reported by many researchers that coercivity depends on many factors like magnetic anisotropy, magnetic phase composition, particle size, and particle shape [70]. Based on a study performed by Zhao et al. [71] on $CoFe_2O_4$/MgO nanocomposites, it is found that the coercivity of the nanocomposite is much larger than that of pure $CoFe_2O_4$. This was explained by the pinning effect that takes place at the interface of the two phases. The stability and magnetic behavior of composite materials are

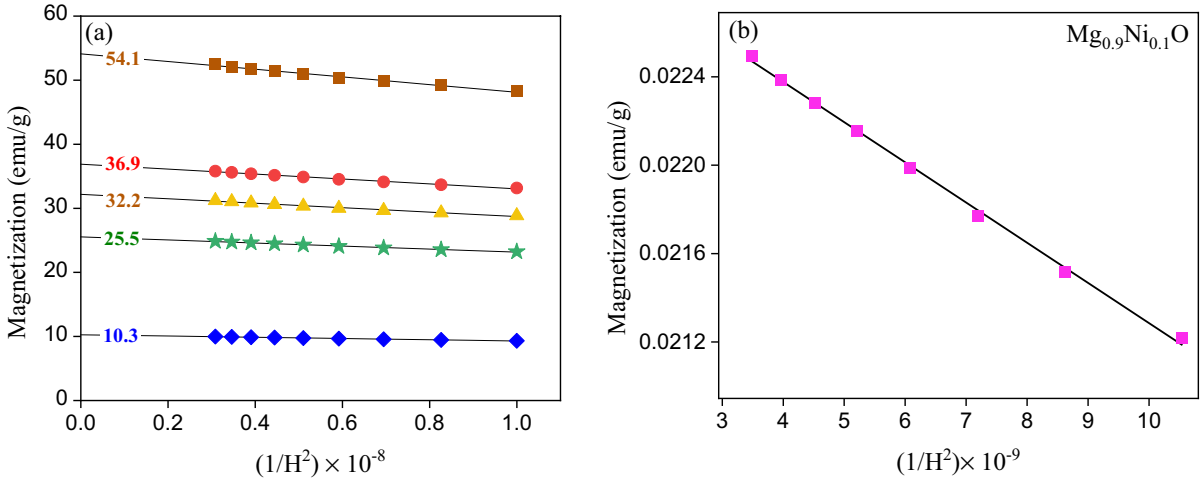

Fig. 10 M versus $1/H^2$ curve extrapolated to $1/H^2 = 0$ for (**a**) x = 0, 0.1, 0.2, 0.4 and 0.8 (**b**) x = 1

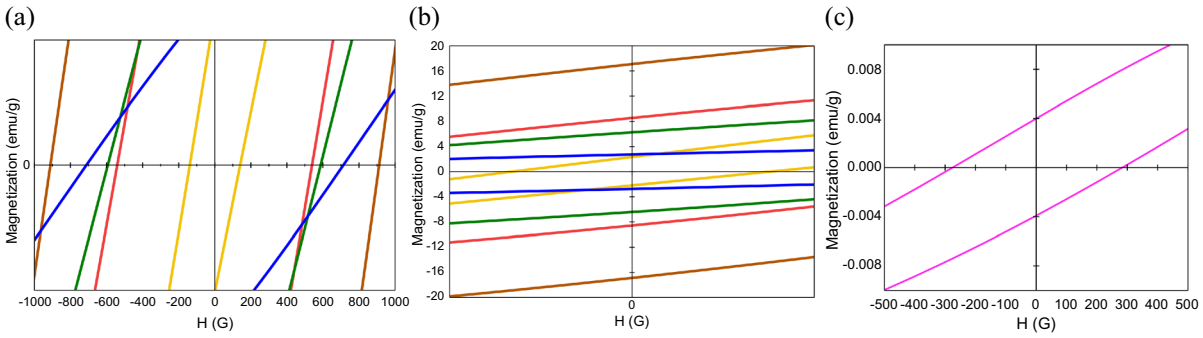

Fig. 11 M versus H plots showing (**a**) H-intercept(H_c) and (**b**) M-intercept(M_r) for $CoFe_2O_4$, CM10, CM20, CM40 and CM80 and (**c**) H_c and M_r for $Mg_{0.9}Ni_{0.1}O$

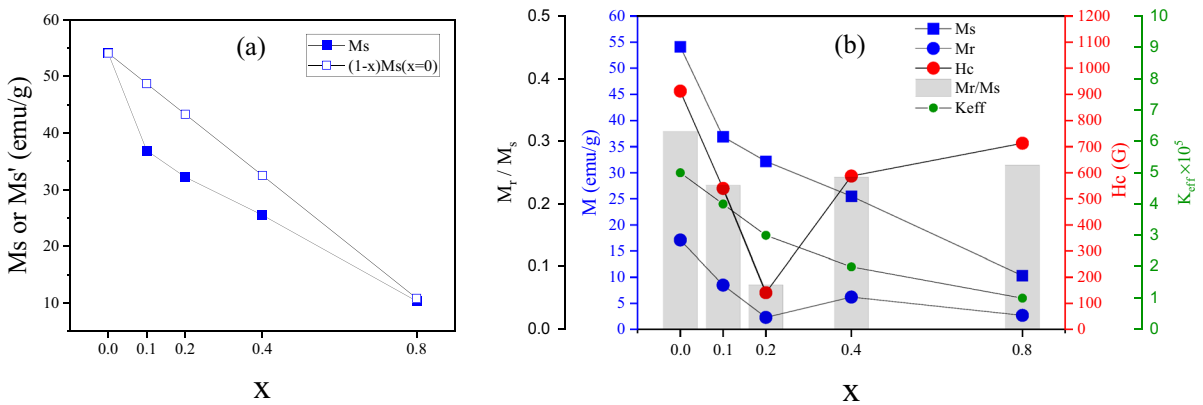

Fig. 12 (**a**) M_s (1-x)M_s(x = 0) and (**b**) M_s, M_r, H_c M_r/M_s and K_{eff} as a function of x (x = 0, 0.1, 0.2, 0.4, 0.8 and 1)

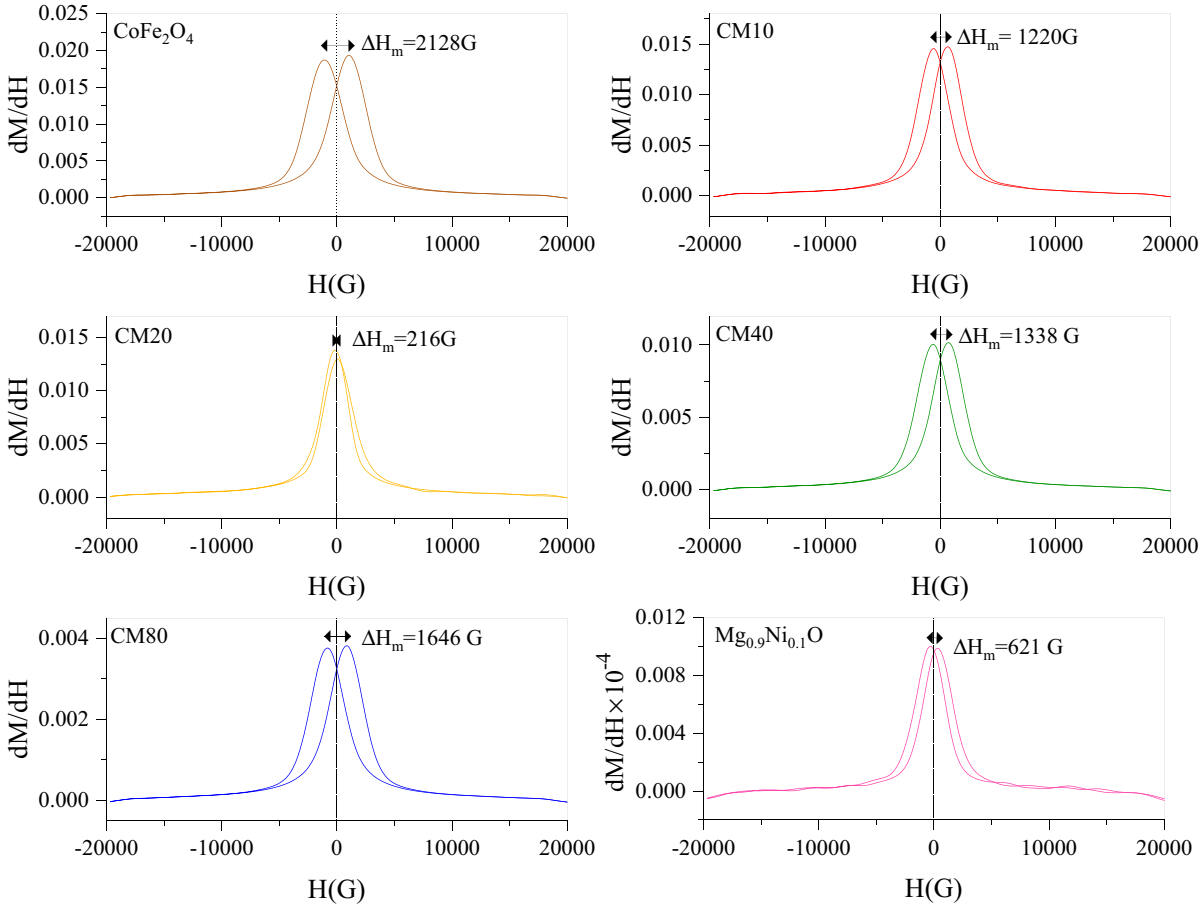

Fig. 13 The dM/dH vs. H plots of x = 0, x = 0.1,x = 0.2, x = 0.4 and x = 0.8, in addition to H_c and H_m as a function of x

impacted by this phenomenon. By adding another energy barrier, it modifies the motion of magnetic domain walls, increasing the material's coercivity in the process. Another study was performed by Xi et al. [36] on the influence of MgO on the magnetic properties of $CoFe_2O_4$ and observed a decrease (low MgO content) and then an increase (higher MgO content) in the coercivity of the $CoFe_2O_4$/MgO nanocomposites which is similar to our case. Additionally, Manh et al. [31] suggested that the significant change in coercivity can be associated with Co^{2+} distribution between A and B sites, and this is also confirmed in XRD, Raman, and XPS analysis. The remanence ratio M_r/M_s serves as the distinctive parameter for magnetic materials, offering insights into how the magnetization direction realigns with the nearest easy axis direction after switching off the magnetic field [72]. The M_r/M_s ratio of $CoFe_2O_4$, CM10, CM20, CM40, and CM80 shows a similar trend as the coercivity, as seen in Fig. 12. This is because a greater demagnetizing field is needed to reduce the magnetization to zero when the M_r/M_s ratio is higher [42]. All the values are less than 0.5 which is an indication of the anisotropic nature of the nanoparticles as reported by Yadav et al. [41]. The lowest ratio was for CM20 (0.071) confirming that these nanoparticles can be used for magnetic fluids [73]. CM80, however, had the greatest ratio of all four nanocomposites; this could be because the dipolar interaction between the embedded CoFe2O4 nanoparticles and Mg0.9Ni0.1O nanoparticles is enhanced.

For deeper magnetic investigation, the evaluation of the interphase exchange coupling between the two phases can be accomplished by examining the demagnetization curves (dH/dM vs. H). These

curves were generated at room temperature and depicted in Fig. 13. All the curves show one peak on each side of H = 0, and this is evidence of exchange coupling between the $CoFe_2O_4$ and $Mg_{0.9}Ni_{0.1}O$ phases [74]. It is well known that the better the exchange coupling the narrower the peak is and vice versa [75]. The width of the peaks seems to decrease from x = 0 to x = 0.2 and then increases from x = 0.2 to x = 0.8. As a result, the maximum and minimum exchange coupling, in the four nanocomposites, are for CM20 and CM80, respectively. It can be seen that the two peaks observed in each plot are almost symmetrical around H = 0 and separated by a magnetic field $2H_m$, where H_m represents the inflection point in the M-H loop, and it is almost very close to the coercivity (H_c) of the material [76]. The values of H_m and H_c are plotted as a function of x in Fig. 14. H_m values are all greater than the coercivity (H_c) except for the CM20 nanocomposite. The larger values of H_m than H_c indicate the switch field distribution due to disordered shell contributions in pseudo-single domain or multi-domain grains [77]. However, smaller values for H_m are due to the absence of switch field distribution [78].

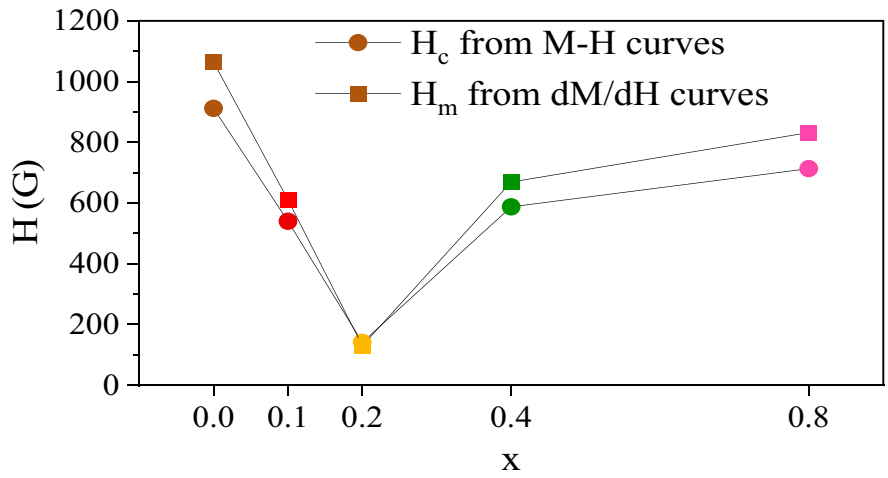

Fig. 14 H_c and H_m as a function of x for x = 0, 0.1, 0.2, 0.4 qnd 0.8

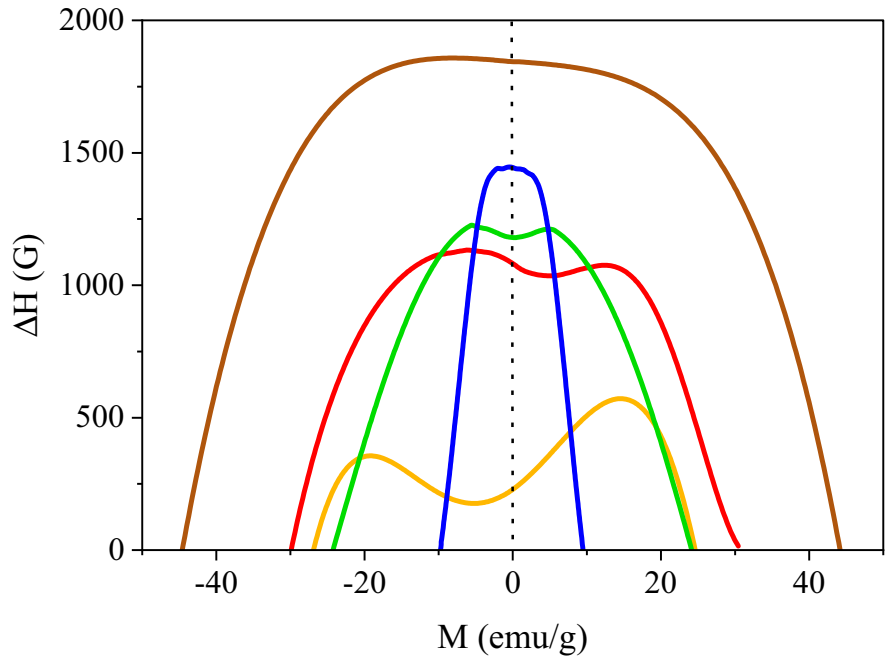

Fig. 15 Loop width versus magnetization for x = 0, 0.1, 0.2, 0.4 qnd 0.8

The width of the loops (ΔH) has been plotted against the magnetization in Fig. 15 to provide a clear picture of the magnetic interactions in the nanocomposites. The loop width is obtained by the subtraction of –ve from + ve applied magnetic field. Interestingly, the shape of the ΔH vs. M plots changes with the increase in the weight percentage of the $Mg_{0.9}Ni_{0.1}O$ phase. For $CoFe_2O_4$, it is a bell shape, and then it changes to a bell shape with a dip inside for CM10, CM20, and CM40 nanocomposites. That is to say, the maximum value for ΔH is not at zero magnetization. Surprisingly, the dip disappears in CM80, and it becomes like that of $CoFe_2O_4$ but with a narrower width. Many researchers reported that the appearance of the dip is attributed to exchange bias between different magnetic materials in the nanocomposites [79–81]. Pandey et al. [80] have related the biasing between different magnetic phases in nanocomposites to occur mostly in the ball milling method rather than the solid-state method. The reason is that during ball milling, used in this work, the different phases come closer to each other so that the magnetic interaction can be more noticed. Based on ΔH vs. M plots, one can conclude that the magnetic interaction is minimum in CM80 and maximum in CM20. This is also confirmed in the dM/dH curves analysis. Interestingly, it is observed that the highest is the dip, the largest is the coercivity, and vice versa. This could be explained as follows: The domain walls of the $Mg_{0.9}Ni_{0.1}O$ phase move towards the interface between the two phases due to the high magnetic interaction for the relatively small weight fraction of $Mg_{0.9}Ni_{0.1}O$ phase (CM10 and CM20). This phenomenon is associated with the magnetization reversal of $CoFe_2O_4$, which results in a decrease in the sample's coercivity when compared to the pure phase [82]. However, for a high weight % of $Mg_{0.9}Ni_{0.1}O$ (CM40 and CM80), the magnetic interaction between the two phases is weak, and the coercivity increases again [83]. MgO doped with nickel demonstrates strong adsorption capabilities [57], making it a promising choice for adsorption applications when combined with magnetic $CoFe_2O_4$ in a nanocomposite like CM80. This composite offers very efficient adsorption since it is easily removed from water using a simple magnetic method. A table summarizing various research findings on $CoFe_2O_4$/oxide nanocomposites can be seen below (Table 3).

Table 3 Previous studies that have been done on $CoFe_2O_4$/oxide nanocomposites with some results and applications, where NC, SP, NM, Pa, Fi, Da, WFe and Fe stand for nanocomposite, super paramagnetic, non magnetic, paramagnetic, ferrimagnetic, diamagnetic, weak ferromagnetic and ferromagnetic, repectively

Year	Nanocomposite	Preparation method	Particle size/Shape			Magnetic behavior			Application	Ref
			Ferrite	Oxide	NC	Ferrite	Oxide	NC		
2013	$CoFe_2O_4/TiO_2$	microwave-hydrothermal method + Ball milling	18nm	22nm	[20nm,30nm]	SP	NM	SP	Thermal variation of dielectric constant at constant frequency	[84]
2015	$CoFe_2O_4/ZnO$	Combustion reaction method	55nm	60nm	----	Fi	Da	Pa to Fi	---	[85]
2017	$CoFe_2O_4/GO$	modified Hummers method	Steel-like structure			---	---	---	Adsorption of Pb(II) ions	[86]
2018	$CoFe_2O_4/BaTiO_3$	solid-state method + ball milling	----	---	----	Fe	WFe	Fe	---	[87]
2020	$CoFe_2O_4/MgO$	sol–gel auto-combustion	----	---	37.6nm	WFe	---	WFe	Non-contact sensors and actuators with low-magnetic field	[36]
2021	$CoFe_2O_4/GO$	co-precipitation method	----	---	----	---	---	---	Nuclear waste remediation	[88]
Present study	$CoFe_2O_4/Mg_{0.9}Ni_{0.1}O$	co-precipitation method + Ball milling	14.7nm	40.9	[25nm,57nm]	Fe	WFe + Pa	Fe	Adsorption / magnetic fluids	---

Conclusion

The co-precipitation technique followed by a high-speed ball milling procedure has succeeded in the co-synthesis of pure $CoFe_2O_4$ and $Mg_{0.9}Ni_{0.1}O$ phases with their four nanocomposites. The XRD analysis showed high crystallinity and purity for the synthesized samples without the formation of any secondary phases. The TEM micrographs showed spherical nanoparticles for all samples with maximum particle size for x = 0.8. The d-spacing obtained from HRTEM micrographs confirmed the formation of the two pure phases as well as their nanocomposites. The Raman spectra showed sharp peaks for $CoFe_2O_4$ and CM40 samples with cation redistribution between these two phases. $Mg_{0.9}Ni_{0.1}O$ Raman spectrum had a very clear high-intensity peak in the pure sample, and it appeared much smaller in the nanocomposites. Moreover, in XPS, the chemical states of the elements of both pure samples and CM40 nanocomposite were analyzed, demonstrating the composition elements (Co^{2+}, Fe^{2+}, Fe^{3+}, Mg^{2+}, O^{2-} and Ni^{2+}). Finally, the magnetic study of the different samples revealed the soft ferromagnetic behavior for the pure $CoFe_2O_4$ phase and the very weak ferromagnetism in pure $Mg_{0.9}Ni_{0.1}O$. The nanocomposites followed a clear decreasing trend in the saturation magnetization with the addition of the $Mg_{0.9}Ni_{0.1}O$ phase. The coercivity and M_r/M_s attained maximum values for pure $CoFe_2O_4$ and CM80 nanocomposite. However, the lowest values were recorded for CM20 nanocomposite. As a result, the $Mg_{0.9}Ni_{0.1}O$ phase had a significant effect on the structural and magnetic properties of $CoFe_2O_4$ nanoparticles.

Acknowledgements The authors declare their genuine gratitude and appreciation to the Advanced Materials Science Lab at BAU in Lebanon, the Faculty of Science at Alexandria University in Egypt, and the Central Metallurgical Research & Development Institute (Helwan, Egypt).

Author contributions All authors contributed to the study conception and design. Materials preparation, data collection and analysis were performed by Majed Sharrouf. The first draft of the manuscript was written by Majed Sharrouf and all authors commented on previous versions of the manuscript. All authors read and approved the final version.

Funding The authors did not receive support from any organization for the submitted work.

Data availability No datasets were generated or analysed during the current study.

Declarations

Conflict of interest The authors declare no competing interests.

References

1. Mallesh S, Srinivas V (2019) A comprehensive study on thermal stability and magnetic properties of MnZn-ferrite nanoparticles. J Magn Magn Mater 475:290–303. https://doi.org/10.1016/j.jmmm.2018.11.052
2. Mallesh S, Mondal P, Kavita S, Srinivas V, Nam Y-W (2022) Effect of Ni substitution and annealing temperature on structural and magnetic properties of MnZn-Ferrites: Cytotoxicity study of ZnO and SiO_2 coated core shell structures. Appl Surf Sci 605:154648. https://doi.org/10.1016/j.apsusc.2022.154648
3. Bhame SD, Joy PA (2018) Enhanced strain sensitivity in magnetostrictive spinel ferrite $Co_{1-x}Zn_xFe_2O_4$. J Magn Magn Mater 447:150–154. https://doi.org/10.1016/j.jmmm.2017.09.075
4. Sattler KD (ed) (2010) Handbook of nanophysics: nanoelectronics and nanophotonics. CRC Press, Boca Raton. https://doi.org/10.1201/9781420075519
5. Ebrahimi Z, Hedayati K, Ghanbari D (2017) Preparation of hard magnetic $BaFe_{12}O_{19}$–TiO_2 nanocomposites: applicable for photo-degradation of toxic pollutants. J Mater Sci: Mater Electron 28(18):13956–13969. https://doi.org/10.1007/s10854-017-7245-3
6. Hameed TA, Azab AA, Ibrahim RS, Rady KE (2022) Optimization, structural, optical and magnetic properties of $TiO_2/CoFe_2O_4$ nanocomposites. Ceram Int 48(14):20418–20425. https://doi.org/10.1016/j.ceramint.2022.03.327
7. Alharbi FF et al (2023) Investigation of photoreduction of Cr (VI) and electrocatalytic properties of hydrothermally produced novel $CoFe_2O_4$/ZnO nanostructure. Solid State Sci 143:107278. https://doi.org/10.1016/j.solidstatesciences.2023.107278
8. Hooda N, Sharma R, Hooda A, Khasa S (2022) Investigations on structure, dielectric and multiferroic behavior of (1–x)BaFe12O19–(x)BaTiO3 composites. J Mater Sci: Mater Electron 33(20):16441–16465. https://doi.org/10.1007/s10854-022-08537-7
9. Razavi FS, Ghanbari D, Salavati-Niasari M (2022) Comparative study on the role of noble metal nanoparticles (Pt and Pd) on the photocatalytic performance of the $BaFe_{12}O_{19}$/TiO_2 magnetic nanocomposite: green synthesis, characterization, and removal of organic dyes under visible light. Ind Eng Chem Res 61(36):13314–13327. https://doi.org/10.1021/acs.iecr.2c01066
10. MoslehiNiasar M, Molaei MJ, Aghaei A (2021) Electromagnetic wave absorption properties of barium ferrite/reduced graphene oxide nanocomposites. Int J Eng 34(6):1503–1511. https://doi.org/10.5829/ije.2021.34.06c.14
11. Hosseini SM, Rafiei N, Salabat A, Ahmadi A (2020) Fabrication of new type of barium ferrite/copper oxide composite nanoparticles blended polyvinylchloride based heterogeneous ion exchange membrane. Arab J

Chem 13(1):2470–2482. https://doi.org/10.1016/j.arabjc.2018.06.001
12. Artus M et al (2008) Synthesis and magnetic properties of ferrimagnetic $CoFe_2O_4$ nanoparticles embedded in an antiferromagnetic NiO matrix. Chem Mater 20(15):4861–4872. https://doi.org/10.1021/cm702464e
13. Süngü Mısırlıoğlu B, Kurt V, Çalık H, Çakır Ö, Çakır Koç R (2023) Toxicity and energy storage properties of magnesium oxide doped cobalt ferrite nanocomposites for biomedical applications. Appl Phys A 129. https://doi.org/10.1007/s00339-023-06792-x
14. Mohan R, Ghosh MP, Mukherjee S (2019) The exchange bias effect in $CoFe_2O_4$/NiO nanocomposites prepared by chemical co-precipitation method. Mater Res Express 6(5):056105. https://doi.org/10.1088/2053-1591/ab038c
15. Toksha BG, Shirsath SE, Patange SM, Jadhav KM (2008) Structural investigations and magnetic properties of cobalt ferrite nanoparticles prepared by sol–gel auto combustion method. Solid State Commun 147(11):479–483. https://doi.org/10.1016/j.ssc.2008.06.040
16. Mallesh S, Prabu D, Srinivas V (2017) Thermal stability and magnetic properties of $MgFe_2O_4$@ZnO nanoparticles. AIP Adv 7(5):056103. https://doi.org/10.1063/1.4975355
17. Goryczka T, Dercz G, Prusik K, Pająk L, Łągiewka E (2010) Crystallite size determination of MgO nanopowder from x-ray diffraction patterns registered in GIXD technique. Solid State Phenom 163:177–182. https://doi.org/10.4028/www.scientific.net/SSP.163.177
18. Rajendran V, Deepa B, Mekala R (2018) Studies on structural, morphological, optical and antibacterial activity of pure and Cu-doped MgO nanoparticles synthesized by co-precipitation method. Materials Today: Proceedings 5(2, Part 3):8796–8803. https://doi.org/10.1016/j.matpr.2017.12.308
19. Sierra-Fernandez A et al (2017) Synthesis, photocatalytic, and antifungal properties of MgO, ZnO and Zn/Mg oxide nanoparticles for the protection of calcareous stone heritage. ACS Appl Mater Interfaces 9(29):24873–24886. https://doi.org/10.1021/acsami.7b06130
20. SowriBabu K, Ramachandra Reddy A, Venugopal Reddy K (2015) Green emission from ZnO–MgO nanocomposite due to Mg diffusion at the interface. J Lumin 158:306–312. https://doi.org/10.1016/j.jlumin.2014.10.027
21. Sola D, Oliete PB, Merino RI, Peña JI (2019) Directionally solidified Ni doped MgO-MgSZ eutectic composites for thermophotovoltaic devices. J Eur Ceram Soc 39(4):1206–1213. https://doi.org/10.1016/j.jeurceramsoc.2018.12.032
22. Zhang Z, Zhao Y, Zhu M (2006) NiO films consisting of vertically aligned cone-shaped NiO rods. Appl Phys Lett 88(3):033101. https://doi.org/10.1063/1.2166479
23. Przybylski M, Grabowski J, Zavaliche F, Wulfhekel W, Scholz R, Kirschner J (2002) Structural and magnetic characterization of single-crystalline Fe/MgO/Fe magneto-tunnel junctions grown on GaAs(001) and InP(001). J Phys D: Appl Phys 35(15):1821. https://doi.org/10.1088/0022-3727/35/15/301
24. Taşer A, Güldüren ME, Güney H (2021) Tuning PL emission energy and bandgap with Ni dopant of MgO thin films. Ceram Int 47(11):15792–15800. https://doi.org/10.1016/j.ceramint.2021.02.151
25. Almontasser A, Parveen A (2022) Probing the effect of Ni, Co and Fe doping concentrations on the antibacterial behaviors of MgO nanoparticles. Sci Rep 12(1):1. https://doi.org/10.1038/s41598-022-12081-z
26. Jalili H, Aslibeiki B, Varzaneh AG, Chernenko VA (2019) The effect of magneto-crystalline anisotropy on the properties of hard and soft magnetic ferrite nanoparticles. Beilstein J Nanotechnol 10(1):1348–1359. https://doi.org/10.3762/bjnano.10.133
27. Obeid MM, Edrees SJ, Shukur MM (2018) Synthesis and characterization of pure and cobalt doped magnesium oxide nanoparticles: Insight from experimental and theoretical investigation. Superlattices Microstruct 122:124–139. https://doi.org/10.1016/j.spmi.2018.08.015
28. Ahlawat A et al (2022) Correlation between spin–phonon coupling and magneto-electric effects in CoFe2O4/PMN-PT nanocomposite: Raman spectroscopy and XMCD study. J Mater Sci: Mater Electron 33(25):19766–19778. https://doi.org/10.1007/s10854-022-08780-y
29. Franco A, Pessoni HVS, Neto FO (2016) Enhanced high temperature magnetic properties of ZnO – CoFe2O4 ceramic composite. J Alloy Compd 680:198–205. https://doi.org/10.1016/j.jallcom.2016.04.110
30. Saccone FD, Ferrari S, Errandonea D, Grinblat F, Bilovol V, Agouram S (2015) Cobalt ferrite nanoparticles under high pressure. J Appl Phys 118(7):075903. https://doi.org/10.1063/1.4928856
31. Manh DH, Thanh TD, Phan TL, Yang DS (2023) Towards hard-magnetic behavior of CoFe2O4 nanoparticles: a detailed study of crystalline and electronic structures, and magnetic properties. RSC Adv 13(12):8163–8172. https://doi.org/10.1039/D3RA00525A
32. Nongjai R, Khan S, Asokan K, Ahmed H, Khan I (2012) Magnetic and electrical properties of In doped cobalt ferrite nanoparticles. J Appl Phys 112(8):084321. https://doi.org/10.1063/1.4759436
33. Qin W, Nagase T, Umakoshi Y, Szpunar JA (2008) Relationship between microstrain and lattice parameter change in nanocrystalline materials. Philos Mag Lett 88(3):169–179. https://doi.org/10.1080/09500830701840155
34. Adeela N et al (2015) Influence of manganese substitution on structural and magnetic properties of $CoFe_2O_4$ nanoparticles. J Alloy Compd 639:533–540. https://doi.org/10.1016/j.jallcom.2015.03.203
35. Rao KG, Ashok CH, Rao KV, Chakra CS (2014) Structural properties of MgO nanoparticles: synthesized by co-precipitation technique. Int J Sci Res 3(12):43–46
36. Xi G, Heng X, Dun C, Zhang Y (2020) The influence of MgO on the magnetic and magnetostrictive properties of $CoFe_2O_4$ nanoparticles synthesized using spent LIBs. Physica B 589:412182. https://doi.org/10.1016/j.physb.2020.412182
37. Kumar Y, Sharma A, Shirage PM (2019) Impact of different morphologies of $CoFe_2O_4$ nanoparticles for tuning of structural, optical and magnetic properties. J Alloy Compd 778:398–409. https://doi.org/10.1016/j.jallcom.2018.11.128
38. Mishra A, Singh V, Mohanty T (2017) Coexistence of interfacial stress and charge transfer in graphene oxide based magnetic nanocomposites. J Mater Sci 52(13):7677–7687. https://doi.org/10.1007/s10853-017-1062-1
39. Patel M et al (2013) Antibacterial and cytotoxic effect of magnesium oxide nanoparticles on bacterial and human cells. J Nanoeng Nanomanuf 3:162–166. https://doi.org/10.1166/jnan.2013.1122

40. Chandramohan P, Srinivasan MP, Velmurugan S, Narasimhan SV (2011) Cation distribution and particle size effect on Raman spectrum of $CoFe_2O_4$. J Solid State Chem 184(1):89–96. https://doi.org/10.1016/j.jssc.2010.10.019
41. Yadav RS et al (2017) Impact of grain size and structural changes on magnetic, dielectric, electrical, impedance and modulus spectroscopic characteristics of $CoFe_2O_4$ nanoparticles synthesized by honey mediated sol-gel combustion method. Adv Nat Sci: Nanosci Nanotechnol 8(4):045002. https://doi.org/10.1088/2043-6254/aa853a
42. Kumar Y, Shirage PM (2017) Highest coercivity and considerable saturation magnetization of $CoFe_2O_4$ nanoparticles with tunable band gap prepared by thermal decomposition approach. J Mater Sci 52(9):4840–4851. https://doi.org/10.1007/s10853-016-0719-5
43. Ansari SM et al (2020) Eco-friendly synthesis, crystal chemistry, and magnetic properties of manganese-substituted $CoFe_2O_4$ nanoparticles. ACS Omega 5(31):19315–19330. https://doi.org/10.1021/acsomega.9b02492
44. Weibel A, Mesguich D, Chevallier G, Flahaut E, Laurent C (2018) Fast and easy preparation of few-layered-graphene/magnesia powders for strong, hard and electrically conducting composites. Carbon 136:270–279. https://doi.org/10.1016/j.carbon.2018.04.085
45. Athar T, Deshmukh A, Ahmed W (2012) Synthesis of MgO nanopowder viaNon aqueous sol-gel method. Adv Sci Lett 5:1–3. https://doi.org/10.1166/asl.2012.2190
46. Ortiz-Quiñonez J-L, Pal U, Villanueva MS (2018) Structural, magnetic, and catalytic evaluation of spinel Co, Ni, and Co–Ni ferrite nanoparticles fabricated by low-temperature solution combustion process. ACS Omega 3(11):14986–15001. https://doi.org/10.1021/acsomega.8b02229
47. Suthar M, Bapna K, Kumar K, Ahuja BL (2018) Structural study of Mg doped cobalt ferrite thin films on ITO coated glass substrate. 1953:100046. https://doi.org/10.1063/1.5032982
48. Tong Z et al (2021) Effects of Ni-doping on microstructure, magnetic and microwave absorption properties of CoFe2O4. Mater Sci Eng, B 268:115092. https://doi.org/10.1016/j.mseb.2021.115092
49. Kim K, Park J (2019) Spectroscopic investigation on tetrahedral Co^{2+} in thin-film $CoFe_2O_4$. J Sol-Gel Sci Technol 92(1):40–44. https://doi.org/10.1007/s10971-019-05099-9
50. Swathi S, Yuvakkumar R, Kumar PS, Ravi G, Velauthapillai D (2021) Annealing temperature effect on cobalt ferrite nanoparticles for photocatalytic degradation. Chemosphere 281:130903. https://doi.org/10.1016/j.chemosphere.2021.130903
51. Li R, Sun C, Liu J, Zhen Q (2017) Sulfur-doped $CoFe_2O_4$ nanopowders for enhanced visible-light photocatalytic activity and magnetic properties. RSC Adv 7:50546–50554. https://doi.org/10.1039/C7RA10016G
52. Yu J et al (2018) Bifunctionality from synergy: CoP nanoparticles embedded in amorphous CoO_x nanoplates with heterostructures for highly efficient water electrolysis. Adv Sci 5. https://doi.org/10.1002/advs.201800514
53. Chen X, Wu C, Guo Z (2019) Synthesis of efficient Cu/$CoFe_2O_4$ catalysts for low temperature CO oxidation. Catal Lett 149. https://doi.org/10.1007/s10562-018-2612-0
54. Ahamad T, Naushad M, Ubaidullah M, Alshehri S (2020) Fabrication of highly porous polymeric nanocomposite for the removal of radioactive U(VI) and Eu(III) ions from aqueous solution. Polymers (Basel) 12(12):2940. https://doi.org/10.3390/polym12122940
55. Ikeuba AI, Zhang B, Wang J, Han E-H, Ke W, Okafor PC (2018) SVET and SIET study of galvanic corrosion of Al/$MgZn_2$ in aqueous solutions at different pH. J Electrochem Soc 165(3):C180–C194. https://doi.org/10.1149/2.0861803jes
56. Yang Z-G, Zhu L-P, Guo Y-M, Ye Z-Z, Zhao B-H (2011) Preparation and band-gap modulation in $Mg_xNi_{1-x}O$ thin films as a function of Mg contents. Thin Solid Films 519(15):5174–5177. https://doi.org/10.1016/j.tsf.2011.01.082
57. Hunpratub S, Phokha S, Kidkhunthod P, Chanlek N, Chindaprasirt P (2021) The effect of cation distribution on the magnetic properties of $CoFe_2O_4$ nanoparticles. Results in Physics 24:104112. https://doi.org/10.1016/j.rinp.2021.104112
58. Li X et al (2020) Size-effect induced cation redistribution on the magnetic properties of well-dispersed $CoFe_2O_4$ nanocrystals. J Alloy Compd 841:155710. https://doi.org/10.1016/j.jallcom.2020.155710
59. Jian G, Fu Q, Zhou D (2012) Particles size effects of single domain $CoFe_2O_4$ on suspensions stability. J Magn Magn Mater 324(5):671–676. https://doi.org/10.1016/j.jmmm.2011.08.036
60. Hammad A, Darwish A-F, El Nahrawy AM (2020) Identification of dielectric and magnetic properties of core shell ZnTiO3/CoFe2O4 nanocomposites. Appl Phys A 126. https://doi.org/10.1007/s00339-020-03679-z
61. Narayan J, Nori S, Ramachandran S, Prater JT (2009) The synthesis and magnetic properties of a nanostructured Ni-MgO system. JOM 61(6):76–81. https://doi.org/10.1007/s11837-009-0093-8
62. Almessiere MA, Slimani Y, Baykal A (2018) Structural and magnetic properties of Ce-doped strontium hexaferrite. Ceram Int 44(8):9000–9008. https://doi.org/10.1016/j.ceramint.2018.02.101
63. Seehra MS, Suri S, Singh V (2012) Effects of Cu doping on the magnetism of CeO_2 nanoparticles. J Appl Phys 111(7):07B516. https://doi.org/10.1063/1.3676223
64. Ali K, Iqbal J, Jana T, Ahmad N, Ahmad I, Wan D (2017) Enhancement of microwaves absorption properties of $CuFe_2O_4$ magnetic nanoparticles embedded in MgO matrix. J Alloy Compd 696:711–717. https://doi.org/10.1016/j.jallcom.2016.10.220
65. Cao J et al (2009) Large-scale synthesis and microwave absorption enhancement of actinomorphic tubular ZnO/$CoFe_2O_4$ nanocomposites. J Phys Chem B 113(14):4642–4647. https://doi.org/10.1021/jp8093287
66. Li F, Yang Q, Evans DG, Duan X (2005) Synthesis of magnetic nanocomposite MgO/$MgFe_2O_4$ from Mg-Fe layered double hydroxides precursors. J Mater Sci 40(8):1917–1922. https://doi.org/10.1007/s10853-005-1211-9
67. Kumar Y, Sharma A, Ahmed MA, Mali SS, Hong CK, Shirage PM (2018) Morphology-controlled synthesis and enhanced energy product (BH)max of $CoFe_2O_4$ nanoparticles. New J Chem 42(19):15793–15802. https://doi.org/10.1039/C8NJ02177E

68. Liu BH, Ding J, Dong ZL, Boothroyd CB, Yin JH, Yi JB (2006) Microstructural evolution and its influence on the magnetic properties of $CoFe_2O_4$ powders during mechanical milling. Phys Rev B 74(18):184427. https://doi.org/10.1103/PhysRevB.74.184427
69. Mund HS, Ahuja BL (2017) Structural and magnetic properties of Mg doped cobalt ferrite nano particles prepared by sol-gel method. Mater Res Bull 85:228–233. https://doi.org/10.1016/j.materresbull.2016.09.027
70. Feng WC, Li W, Liu XM, Liu T, Li XM (2007) Phase distribution, grain size and coercivity in nanocomposite permanent materials. J Magnet Magnet Mater 310(2, Part 3):2584–2586. https://doi.org/10.1016/j.jmmm.2006.10.1081
71. Zhao YS, Wang M, Ma YQ (2018) Effects of nitriding temperature on the structure and magnetic properties of CoFe2 alloy. J Mater Sci: Mater Electron 29(23):20071–20080. https://doi.org/10.1007/s10854-018-0138-2
72. Gore SK et al (2015) Influence of Bi3+-doping on the magnetic and Mössbauer properties of spinel cobalt ferrite. Dalton Trans 44(14):6384–6390. https://doi.org/10.1039/C5DT00156K
73. Monisha P, Priyadharshini P, Gomathi SS, Mahendran M, Pushpanathan K (2019) Role of Zn dopant on superparamagnetic property of CoFe2O4 nanoparticles. Appl Phys A 125(10):736. https://doi.org/10.1007/s00339-019-3014-x
74. Neupane D, Ghimire M, Adhikari H, Lisfi A, Mishra SR (2017) Synthesis and magnetic study of magnetically hard-soft $SrFe_{12-y}AlyO_{19}$ - x Wt.% Ni0.5Zn0.5Fe2O4 nanocomposites. AIP Adv 7(5):055602. https://doi.org/10.1063/1.4978398
75. Hirian R, Bortnic R, Popa F, Souca G, Isnard O, Pop V (2022) Structural, microstructural and magnetic properties of $SmCo_5$/20wt%Fe magnetic nanocomposites produced by mechanical milling in the presence of CaO. Magnetochemistry 8:124. https://doi.org/10.3390/magnetochemistry8100124
76. Godara SK et al (2022) Sol-gel auto-combustion synthesis of double metal-doped barium hexaferrite nanoparticles for permanent magnet applications. J Solid State Chem 312:123215. https://doi.org/10.1016/j.jssc.2022.123215
77. Kaleemullah NS, Malaidurai M, Thangavel R, Kumar J (2022) Investigation on the structural and magnetic properties of $M_xBi_{2-x}Te_3$ (M = Gd, Fe, Cr) (x = 0, 1) using colloidal hot-injection method. Bull Mater Sci 45(1):53. https://doi.org/10.1007/s12034-021-02632-x
78. Dipesh DN, Wang L, Adhikari H, Alam J, Mishra SR (2016) Influence of Al3+ doping on structural and magnetic properties of $CoFe_{2-x}Al_xO4$ Ferrite nanoparticles. J Alloy Compd 688:413–421. https://doi.org/10.1016/j.jallcom.2016.07.030
79. Manglam MK, Kumari S, Guha S, Datta S, Kar M (2020) Study of magnetic interaction between hard and soft magnetic ferrite in the nanocomposite. AIP Conf Proc 2220(1):110020. https://doi.org/10.1063/5.0001220
80. Pandey R, Kumar Pradhan L, Kumari S, Kumar Manglam M, Kumar S, Kar M (2020) Surface magnetic interactions between $Bi_{0.85}La_{0.15}FeO_3$ and $BaFe_{12}O_{19}$ nanomaterials in $(1-x)Bi_{0.85}La_{0.15}FeO_3/(x)BaFe_{12}O_{19}$ nanocomposites. J Magnet Magnet Mater 508:166862. https://doi.org/10.1016/j.jmmm.2020.166862
81. Manglam MK, Mallick J, Kumari S, Pandey R, Kar M (2021) Crystal structure and magnetic properties study on barium hexaferrite (BHF) and cobalt zinc ferrite (CZF) in composites. Solid State Sci 113:106529. https://doi.org/10.1016/j.solidstatesciences.2020.106529
82. Tavakolinia F, Yousefi M, SeyyedAfghahi SS, Baghshahi S, Samadi S (2018) Synthesis of novel hard/soft ferrite composites particles with improved magnetic properties and exchange coupling. Process Appl Ceram 12:248–256. https://doi.org/10.2298/PAC1803248T
83. Dahal J, Neupane D, Mishra S (2019) Exchange-coupling behavior in SrFe12O19/La0.7Sr0.3MnO3 nanocomposites. Ceramics 2:100–111. https://doi.org/10.3390/ceramics2010010
84. Raju, Murthy PSR (2013) Microwave-hydrothermal synthesis Of $CoFe_2O_4$-TiO_2 nanocomposites. Adv Mater Lett 4(1):99–105. https://doi.org/10.5185/amlett.2013.icnano.130
85. Castro TJ, da Silva SW, Nakagomi F, Moura NS, Franco A, Morais PC (2015) Structural and magnetic properties of ZnO–$CoFe_2O_4$ nanocomposites. J Magn Magn Mater 389:27–33. https://doi.org/10.1016/j.jmmm.2015.04.036
86. Zhao Q et al (2017) Efficient removal of Pb(II) from aqueous solution by $CoFe_2O_4$/Graphene oxide nanocomposite: kinetic, isotherm and thermodynamic. J Nanosci Nanotechnol 17(6):3951–3958. https://doi.org/10.1166/jnn.2017.13100
87. Kumar R, Guha S, Kr. Singh R, Kar M (2018) Surface anisotropy induced magnetism in $BaTiO_3$-$CoFe_2O_4$ (BTO-CFO) nanocomposite. J Magnet Magnet Mater 465:93–99. https://doi.org/10.1016/j.jmmm.2018.05.061
88. Gupta NK, Viltres H, López YC, Salunkhe G, Sengupta A (2021) Magnetic $CoFe_2O_4$/Graphene oxide nanocomposite for highly efficient separation of f-block elements. Surf Interfaces 23:100916. https://doi.org/10.1016/j.surfin.2020.100916